Spring 5-1-2021

Small-Scale Resuspension and Redistribution of Surface Sediments in the Northeast Gulf of Mexico

Austin Harris

SMALL-SCALE RESUSPENSION AND REDISTRIBUTION OF SURFACE SEDIMENTS IN THE NORTHEAST GULF OF MEXICO

by

Austin Harris

A Thesis
Submitted to the Graduate School,
the College of Arts and Sciences
and the School of Ocean Science and Engineering
at The University of Southern Mississippi
in Partial Fulfillment of the Requirements
for the Degree of Master of Science

Approved by:

Dr. Arne R. Diercks, Co-Committee Chair
Dr. Chris Hayes, Co-Committee Chair
Dr. Stephan Howden

May 2021

Published by the Graduate School

ABSTRACT

Following the release of ~4.9 million barrels of oil into the Gulf of Mexico from the Macondo wellhead, a vast area of the seafloor contained recently deposited marine sediments contaminated by the oil spill. The initial deposition of these contaminated marine sediments was likely not the end of the journey for the particles. Downslope gravitational processes and events of increased current speed in the deep ocean setting can result in recently deposited sediments to resuspend and be moved laterally with the current flow, increasing the area effected by the oil spill. Erosion experiments performed in a closed-loop resuspension flume were completed on 23 sediment cores collected from near the Macondo wellhead and areas to the SE. Using flow modeling of the Gulf of Mexico, core sites were chosen to be in areas where erosion or deposition is thought to be the dominant process of that coring location. Sites were reclassified based upon ease of initial transport of material and the shear stress of pulses, or peaks, in eroded sediment volume. All cores had erosion begin at <0.053 dyne cm^{-2} (4.6 cm s^{-1}) and nearly all cores had large pulses of sediment eroded >0.48 dyne cm^{-2} (13.7 cm s^{-1}). Surface sediment characteristics revealed older, rebound material was more easily resuspened than newly deposited material. This suggests that the area effected by the DwH oil spill has increased over time as contaminated material has been transported by natural process to deep waters SE of the wellhead.

ACKNOWLEDGMENTS

I would like to acknowledge my committee members Dr. Arne Diercks, Dr. Chris Hayes, and Dr. Stephan Howden for their feedback and support throughout this research. Especially Dr. Arne Diercks, for taking me on as a graduate student and putting in countless hours helping me grow as a scientist. Many thanks to Kevin Martin and Roy Jarnagin for their help in setting up different aspects of the sediment flume and the great conversations shared. Thank you to the boat crew of the *R/V Point Sur* for their safe operation and the great experience on cruise PS18-25. Lastly, thank you to the members of the REDIRECT project from whom I gained much knowledge from and shared many laughs.

TABLE OF CONTENTS

LIST OF TABLES

LIST OF ILLUSTRATIONS

LIST OF ABBREVIATIONS

DwH	Deepwater Horizon
GoM	Gulf of Mexico
MOS	Marine Oil Snow
BNL	Benthic Nepheloid Layer
TIF	Tagged Image File
MAR	Mass Accumulation Rate
HPG	High-Purity Germanium
IEAE	International Atomic Energy Association
CRS	Constant Rate Supply
%C	Percentage Carbon

CHAPTER I - Introduction

1.1 Deepwater Horizon Oil Spill Background

The Deep Water Horizon (DwH) oil spill released ~4.9 million barrels of crude oil into the Gulf of Mexico (GoM) from April 20th to July 15th, 2010. Another ~7 million liters of chemical dispersants were also introduced into the GoM to catalyze the degradation of the oil. Using available synthetic aperture radar, MacDonald et al., (2015) discovered that the 87-day period of oil release from DwH produced an oil slick that was 11,200 km^2 in surface area and a volume of 22,600 m^3. Of the oil spilled into the GoM, ~75% was accounted for by recovery at the wellhead, burning, chemical dispersing, natural dispersing, and by evaporation or dissolving (Lehr et al., 2010). This research did not include any estimates for the amount of oil removed by settling through the water column and sedimentation on the seafloor. The presence of marine oil snow (MOS) in the surface waters near the Macondo wellhead suggest that the vertical transportation of these large, mucus-rich particles could have been a primary mechanisms for export of contaminants to the deep GoM (Passow et al., 2012; Vonk et al., 2015; Daly et at., 2016). Multiple biological, geological, sedimentological and chemical studies have attempted to quantify the amount of oil that was transported and deposited on the seafloor (Valentine et al., 2014; Brooks et al., 2015; Schwing et al., 2015; Daly et al., 2016 Romero et al., 2017). Results of these studies show a decline in benthic foraminifera density, increased sediment accumulation rates, presence of fossil-carbon in surface sediments, hopane and other hydrocarbon compounds present that reflect DwH oil was in the surface sediments following the spill. Estimates of oil deposition vary from 0.5-21% of the oil was transported to the seafloor along with $1.9 \pm 0.9 * 10^4$ metric tons of hydrocarbons

(Valentine et al., 2014; Chanton et al., 2015; Romero et al., 2017). Increased Mississippi River discharge along with the addition of drilling mud to the wellhead during the spill sourced high amounts of particles for oil to bind with and raise the likelihood of the oil being transported to the seafloor (Brooks et al., 2015; Yan et al., 2016).

1.2 Resuspension of Surficial Marine Sediments

Seafloor heterogeneity along with deep-sea currents have likely redistributed the contaminated sediments, resulting in an affected area larger than initially predicted. Sediments can be redistributed when lateral flow stress overcomes the cohesive properties of the sediments, causing the sediments to be transported into the water column and potentially forming benthic nepheloid layers (BNLs) (Gardner et al., 1983; Lampitt, 1985; McCave, 1986; Thomsen and Gust, 2000; Borrowman et al., 2006; Diercks et al., 2018). The resuspension of the most surficial layer of seafloor sediment has shown varying degrees of resistance depending on the composition of the sediment in the layer (Lampitt, 1985; McCave and Hall, 2006; Gardner et al., 2016). Low-density phytodetritus dominated sediment has shown to be resuspended at the lowest speeds (6-8 cm s^{1}), while non-cohesive silt sized sediments require slightly higher flow speeds (10-15 cm s^{-1}), and sand dominated sediments being resuspended at 25-30 cm s^{-1} (Lampitt, 1985; McCave and Hall, 2006; Gardner et al., 2016). Thomsen and Gust (1999) found on the European continental margin that a more easily resuspendable surface aggregate layer can require flow speeds as low as 0.4-1.2 cm s^{-1} to move this sediment. With low flow speeds transporting surface layer sediments and contributing to BNLs, flow interactions with sea floor structures can be a contributor to near-inertial forcing strong enough to move sediments (Tesi et al., 2012; Turnewitsch et al., 2013; Diercks et al., 2018). This factor is important to consider

especially in the area of DwH, due to numerous salt domes that are present in the northern GoM. Tesi et al., (2012) had results that showed a 60-90% contribution of material to a sediment trap below a flat-topped summit was sourced from the top of the summit. We may see similar sourcing of sediments on lee sides of elevated structures in the GoM, potentially being accumulation zones of contaminated particles originally deposited on the salt domes.

1.3 Gulf of Mexico Watershed Analysis and Bathymetry

With the publication of a new, high-resolution, bathymetrical map of the GoM (Kramer and Shedd, 2017), a watershed analysis of the basin was completed by Dr. Arne Diercks (**Figure 1.1**). This analysis reveals a gradient in the NE GoM that shows gravitational transport is dominantly towards the southeast from the Macondo wellhead.

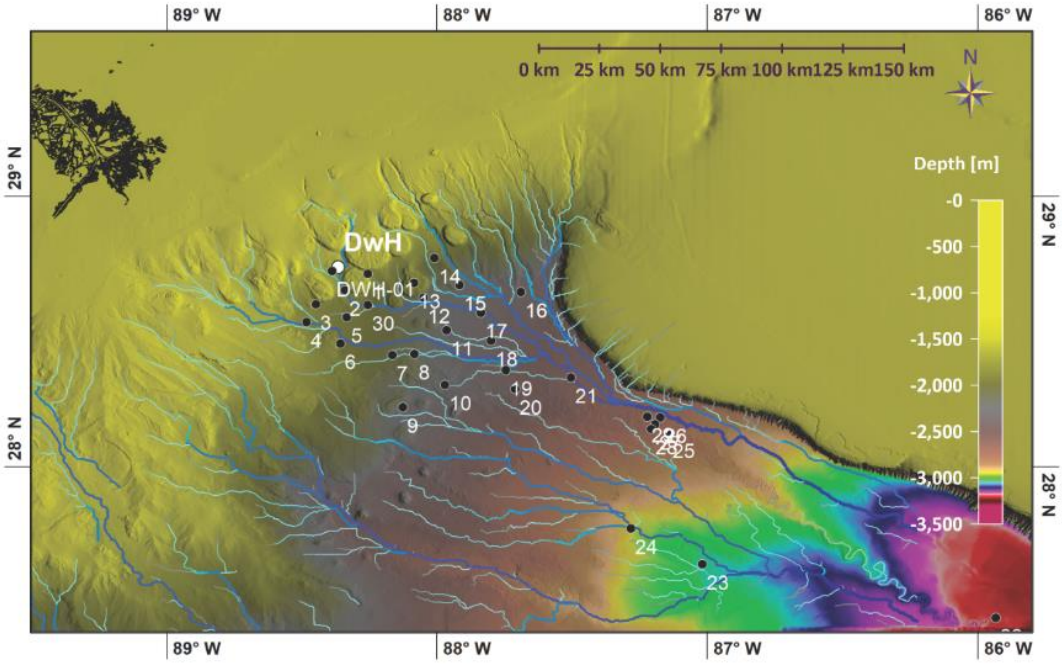

Figure 1.1 *Gulf of Mexico Watershed and REDIRECT Coring Locations*

Map of the NE GoM showing coring locations from cruise PS18-25 on *R/V Point Sur* in May of 2019, overlying drainage pathways modelled from Kramer and Shed (2017) high-resolution bathymetry data. Map credit: Dr. Arne Diercks.

With the surface oil slick covering a large portion of the continental shelf and slope in the northern GoM, sedimentation of hydrocarbons in these areas leave the contaminants vulnerable to be transported downslope to abyssal depths by gravitational processes. A subsurface oil plume also existed in the depth range of the blowout from the drilling pipe (Diercks et al., 2010; Valentine et al., 2014). Contaminated sediments on the slope between 1,000-1,300 m show a "bathtub ring" like deposit of this plume following the blowout, leaving the contaminants susceptible to downhill transport to abyssal depths. Romero et al., 2017 mapped portions of this "bathtub ring" by sampling surface sediments for residual hydrocarbons. **Figure 1.2** shows a map by Romero et al. (2017) with interpolated residual hydrocarbon concentrations, which shows the presence of hydrocarbons in the slope region where the contaminants may be later transported. Gravitational processes have shown to be the dominant delivery mechanism to the abyssal plain for terrigenous sediments (Ward et al., 2017). The Mississippi River is a large source of terrigenous material to the GoM, and was in a high-discharge state during the time of the DwH blowout (Vonk et al., 2015). This was a main contributing factor to the large deposition event during and after the oil spill (Daly et al., 2016; Giering et al., 2018).

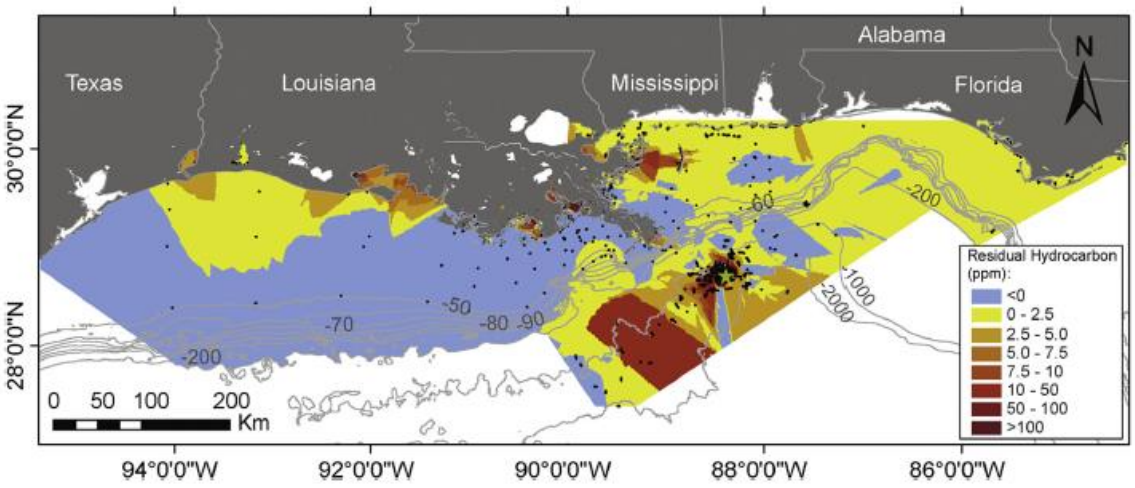

Figure 1.2 *Map of Residual Hydrocarbons in Surface Sediment Sample Following the DwH Oil Spill*

Map of interpolated residual hydrocarbon concentrations (ppm) from surface sediment samples taken from 2010-2011 by Romero et al., 2017. Gray lines indicate bathymetry (m).

1.4 Sediment Flume Background

Sediment flumes are one tool commonly used to gather data involving sediment resuspension and erodibility in-situ and in the laboratory (McNeil et al., 1996; Thomsen and Gust, 1999; Borrowman et al., 2006; Sea Engineering Inc, 2012). Laboratory flume studies give the advantage of being able to control different dynamics in the environment, while in-situ flumes allow scientists to observe sediment dynamics in the natural environment. In-situ flumes face the risk of the natural environment not producing the conditions of primary interest in a specific study (Raven and Gschwend, 1999). Laboratory flumes also add the advantage of being able to collect sediment from numerous locations and environments to examine at a later date, rather than only being able to operate in a single location at a time. Many prior flume experiments have focused river sediments, shallow coastal sediments, or laboratory made sediments mixtures (McNeil et al., 1996; Borrowman et al., 2006; Sea Engineering Inc, 2012). This focus on

shallower sediments is likely due to the higher energy that is consistently present in these environments that transports large volumes of sediment daily. This study is intended to highlight how deep-sea sediment cores respond to increasing shear stress, especially at lower flow speeds. A linear flume was chosen for these experiments primarily due to three factors. Linear flumes have development of fully turbulent flow occurring without the risk of secondary flows that are occasionally present in annular style flumes (Ravens and Gschwend, 1999; Jonnson et al., 2006). A linear flume is also a more easily designed and constructed piece of equipment compared to annular flumes. Finally, in a linear flume it is easier to collect images of down-channel transport in a linear flume, where the test section does not curve or change orientation.

1.5 Sedimentary Environments and Hypotheses

Coring locations for the May 2018 cruise were selected with the focus of analyzing different sedimentary environments in the GoM. The GoM is a unique basin due to its ocean-like structure, containing the major bathymetric provinces of an ocean (coastal zones, continental shelf, slope, and abyssal depths) (Ward et al., 2017). The geographic area for this research has complicated dynamics due to the abundant salt domes present along with incised valleys from prior low-stands in the basin (Ward et al., 2017). This heterogeneity in topographic features likely contributed to the uneven distribution of contaminated sediment deposits following the DwH spill (Ross et al., 2009; Diercks et al., 2018). Coring locations were chosen with two basic environment classifications: erosional and depositional. These classifications were decided based upon structural features and by analyzing the watershed analysis of the GoM. Erosional coring locations were ones in the center of drainage channels from the watershed analysis or on

top of elevated structures. As aforementioned, inertial forces have shown to resuspend sediment on flat-topped summits where they were deposited in less stressed environments (Tesi et al., 2012; Turnewitsch et al., 2013). There have also been recorded instances of flow speeds exceeding 50 cm s^{-1} in channelized features in the GoM under normal forcing conditions (Ross et al., 2009). These instances of high stress events lead to the classification of similar sites as erosional environments. Depositional sites were chosen in areas where stress is expected to be lower and allow for the settling out of suspended particles and potential accumulation of sediment. These sites were either on the lee side of salt domes or other elevated structures where sediments may settle out after being moved from the structures. Other depositional features were chosen due to their proximity to drainage channels from the modelled watershed. **Figure 1.3** (a-e) shows cross sections of two different predicted sedimentary environments. **Figure 1.3** (a & c) show the location of a core taken on the lee side of a salt dome in the GoM. This is an example of what would be considered a deposition site prior to the cruise due to the expected sourcing from the dome and low energy at the base of the lee side of the dome. **Figure 1.3** (b & c) show the location of a submarine channel in GoM. This site would be considered erosional due to the high likelihood of increased flow speeds in this channel resulting in a high-energy environment. Sites outside of these channels or in the open plain of the deep GoM were chosen due to 2 factors: (1) low energy expected in these environments and (2) sourcing of sediments predicted to be from far field resuspension events or pelagic settling from surface waters. The consideration of each of the prior discussed factors lead to 2 working hypotheses for this research.

Hypothesis 1: Cores collected from predicted depocenters in the northern GoM will require lower bed shear stress to initiate the movement of unconsolidated particles on the surface layer in comparison to cores erosional environments.

Hypothesis 2: Erosion of cores collected form predicted depocenters will reveal larger particles are being transported than cores from predicted erosional environments. This will result in differences in the amount of sediment volume eroded and transported throughout experimentation.

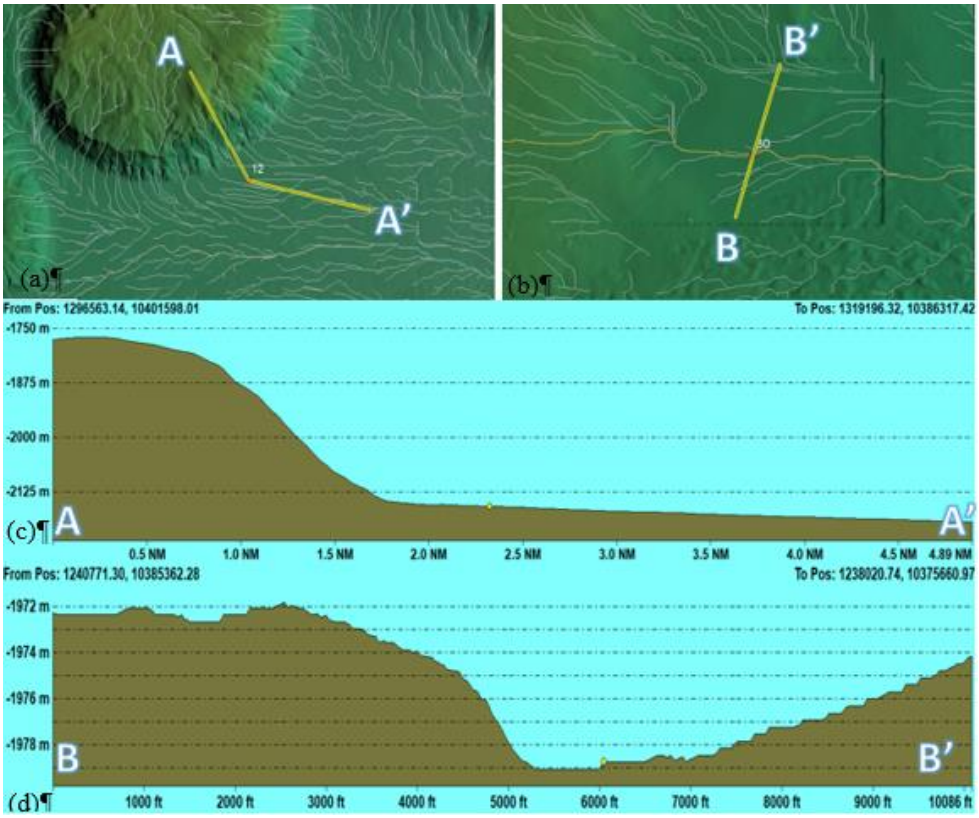

Figure 1.3 *Cross Sections of a Predicted Depositional and Erosional Environment*

This figure shows the cross sections of 2 locations where cores were collected during the PS1825 cruise. (a) & (b) Show mapped areas of the GoM with a salt dome, coring location, and cross section line. Modelled drainage pathways are also on the maps. (c) Shows the cross section from image (a). (d) Shows the plotted cross section from image (b).

1.1 Cruise Details and Core Collection

In May of 2018, 32 sediment multicores were collected on a research cruise in the NE Gulf of Mexico on the *R/V Point Sur*. Water depth at the coring locations varied from 1500 m to >3200 m, with sampling sites starting near the Macondo wellhead and trending to the southeast. **Figure 1.1** shows the cruise track and coring location and **Table 2.1** lists the coring locations with location and depth characteristics. Cores were collected using an Ocean Instruments MC-800 multicorer and were stored in cold storage on the ship. To ensure the integrity of the sediment water interface of the cores, an ample amount of water above the sediment water interface was preserved. **Figure 2.1** shows the intact sediment surface immediately following core collection on the cruise. The presence of a benthic branched organism and lack of turbidity in the overlying water column represent how cores were able to be retrieved with minimal sediment disturbance. To absorb any trapped air inside of the core tube, a sponge was secured at the top of the water, to minimize the sloshing of the water in the tube. Unwanted water movement in the core tube during transport could potentially cause sediment to resuspend and change the core from its natural state.

Upon returning from the cruise, the cores were carefully transported in an upright position, and again stored in a dark refrigerator at 4°C, undisturbed, until experimentation was ready. The storage of cores ranged from three to five months depending on when the core was analyzed in the flume. During this storage period, it is likely that bacterial respiration was occurring as well as alteration of any contaminants that may be present (US EPA., 2001). This may have caused cores to be slightly in a different state during

flume analysis, but it is unknown how storage time of cores affects the resuspension of the sediment. Of the 26 collected multicores, 22 were analyzed for resuspension and erosional characteristics. The multicores that were not analyzed were due to disturbance of the sediment surface during the storage and transportation process. These disturbances reduced the integrity of the sediment water interface and could potentially bias the data that would be collected from these cores.

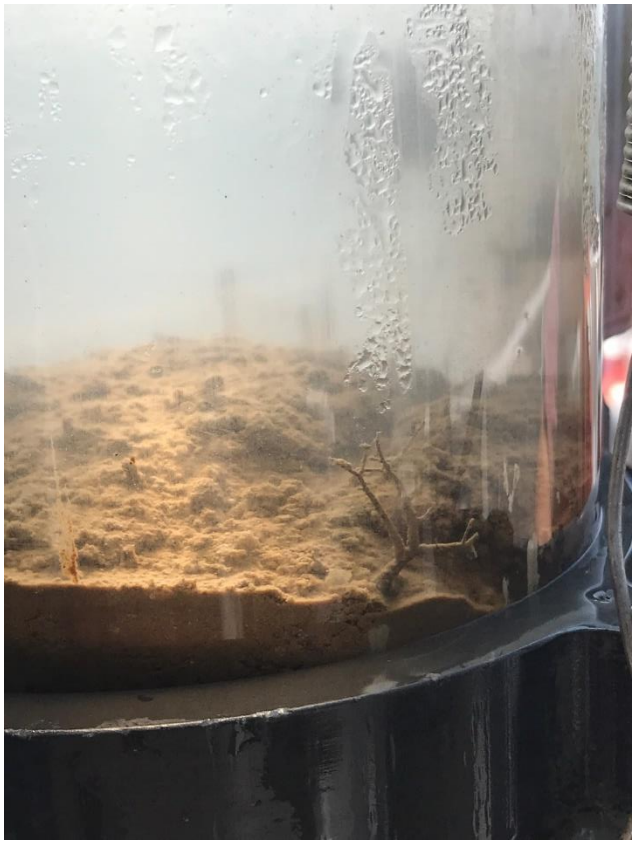

Figure 1.1 *Image of Sediment-water Interfae of a Core Collected during Cruise PS18-25*

This image shows the undisturbed sediment surface from a core collected for resuspension flume analysis. This represents the ability to collect undisturbed cores, preserving the natural setting of the sediment.

Station	Pre-Cruise Sedimentation Environment Classification	Longitude	Latitude	Water Depth (m)
PS1825-MC1	Channel	88° 15.30212' W	28° 42.84920' N	1703
PS1825-MC 2	Depocenter (Lee)	88° 20.35629' W	28° 39.13342' N	1750
PS1825-MC 3	Depocenter (Lee)	88° 26.45617' W	28° 36.04800' N	1730
PS1825-MC 4	Depocenter (Lee)	88° 26.83200' W	28° 32.13078' N	1743
PS1825-MC 5	Depocenter (Lee)	88° 19.11850' W	28° 32.05158' N	1890
PS1825-MC 6	Depocenter (Lee)	88° 21.40813' W	28° 27.32281' N	1910
PS1825-MC 7	Depression	88° 10.07492' W	28° 25.21397' N	2064
PS1825-MC 8	Channel	88° 7.97012' W	28° 24.86423' N	2170
PS1825-MC 9	Depression	88° 7.59109' W	28° 13.25420' N	2272
PS1825-MC 10	Channel	87° 58.23715' W	28° 18.16521' N	2290
PS1825-MC 11	Depression	87° 57.81921' W	28° 30.34882' N	2282
PS1825-MC 12	Depocenter (Lee)	88° 2.94617' W	28° 37.51637' N	2179
PS1825-MC 13	Depression	88° 5.10635' W	28° 40.77679' N	1763
PS1825-MC 14	Channel	88° 0.56992' W	28° 46.33392' N	1946
PS1825-MC 15	Channel (Levee)	87° 54.96780' W	28° 40.34122' N	2410
PS1825-MC 16	Channel (Confluence)	87° 41.40701' W	28° 38.81653' N	2381
PS1825-MC 17	Channel	87° 50.26611' W	28° 34.17881' N	2344
PS1825-MC 18	Channel	87° 47.94754' W	28° 27.95368' N	2393
PS1825-MC 19	Channel	87° 44.67865' W	28° 21.46454' N	2459
PS1825-MC 20	Depression/Plain	87° 42.59766' W	28° 17.28081' N	2448
PS1825-MC 21	Channel (Confluence)	87° 30.24078' W	28° 19.83799' N	2584
PS1825-MC 22	Deep Channel - Erosion – Winnowing	85° 55.97090' W	27° 26.52520' N	3223
PS1825-MC 22A	Deep Channel - Erosion – Winnowing	86° 16.30204' W	27° 30.42636' N	3127
PS1825-MC 23	Depocenter	87° 1.09198' W	27° 38.38956' N	3052
PS1825-MC 24	Depocenter	87° 16.97428' W	27° 46.34078' N	2975
PS1825-MC 30	Depression	88° 15.05768' W	28° 35.76084' N	1986
PS1825-MC 31 (DwH01)	-	88° 23.28094' W	28° 43.50483' N	1570

Table 1.1 *Cruise PS18-25 Core Site Properties*

List of coring station names, pre-cruise sedimentation environments, locations and depths from cruise PS18-25 on *R/V Point Sur*.

1.2 Flume Design and Dynamics

In order to analyze resuspension of the collected sediments, a linear flume was constructed for analysis based on Borrowman et al., (2006) Sedflume design (**Figures 2.2 & 2.3**). The acrylic test section of the flume is 95 cm in length, 15 cm in width, and 5 cm

in height. A DIGITEN, model: FL-1608, Hall Sensor flowmeter, located within the 5 cm PVC pipe before the test section, recorded flow speed throughout each experiment. A 10 cm diameter core opening is located in the center of the flume, 147 cm from the flowmeter. During a test, a Sony 4k camcorder was mounted 20-cm beyond the core, with its focal point set at the center of the channel. This camera collected video data of the sediment being transported down-channel after being eroded from the core. During recording, the camera was unable to resolve any particles that did not exceed 1 pixel in size and was therefore unable to be analyzed during image processing. A GoPro camera was also used to film the surface of the core throughout each experiment. This camera was not used for any statistical analysis due to the inability to manually focus the camera in the flume, but the footage was used to qualitatively analyze the surface of the cores during experimentation. The closed loop flume was filled with filtered artificial salt water (salinity ~ 35) prior to each test, drained, and cleaned after each core. The artificial salt water delivered from the 100 gallon storage tank, first travelled through a 5 cm diameter circular PVC pipe before entering the rectangular test section of the channel through a flow diverter. The full development of turbulent flow was achieved by converting the flow from the 5 cm PVC pipe, through the flow diverter and into the 5 cm tall by 15 cm wide channel. The interaction between the turbulent flow and exposed sediment core surface allowed shear stress to be applied to the core. Shear stress was calculated in the flume and ranged from 0.003 dyne/cm^2 at the lowest flow speed and 1.08 dyne/cm^2 at the highest flow speed. When the resulting shear stress overcomes the cohesive properties of the sediment, erosion begins to occur which can result in the transportation of particles into the camera's view.

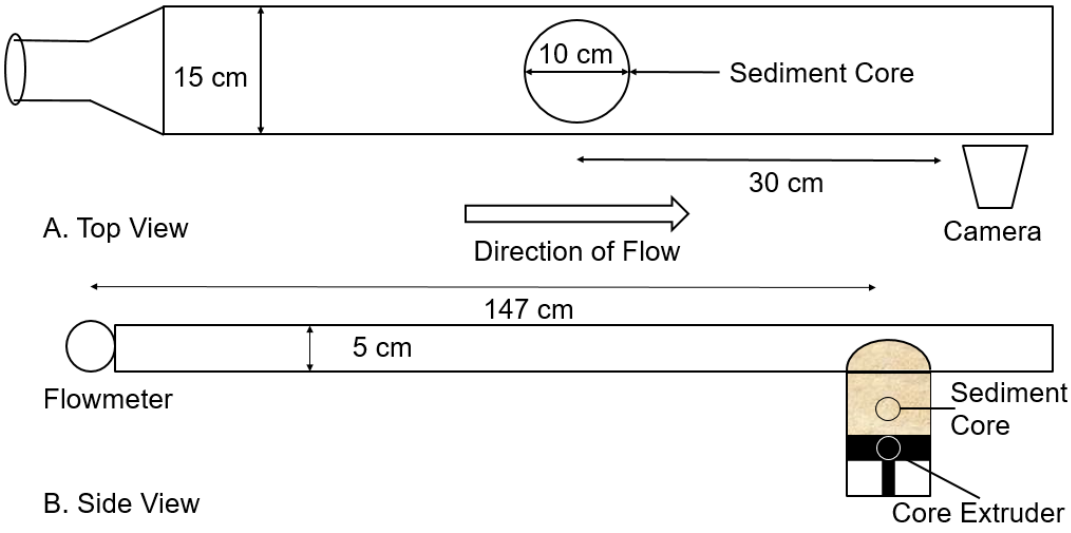

Figure 1.2 *Diagram of Linear Resuspension Flume*

This figure shows the dimensions of the constructed linear sediment flume, as well as the locations of the core insertion, flowmeter, and camera mounting station.

Figure 1.3 *Image of Resuspension Flume*

1.3 Operating Procedure

Cores were carefully introduced into the bottom of the flume channel by using a core extruding mechanism. This mechanism also secured the tube in the flume during the test. While filling the flume, the top of the core tube was covered with a cap to reduce any interaction of the water entering the flume with the sediment surface during the filling process. The sediment water interface inside the core tube was kept as low as possible below the base of the flume to avoid agitation of the sediment interface. Cores were collected and stored with a large amount of original seawater in the core tube. Once the flume was flooded, the protective cover was carefully removed using a pressure equalizing tube in the cover to allow air to escape and water to slowly enter that space. Following the removal of the protective cover, the core material inside the core tube was raised by the core extruder, so that the sediment water interface was flush with the floor of the flume channel. The access hole above the core insertion point in the flume was closed off, producing a closed loop system, and the camera and lighting were prepared for filming. An LED light bar illuminated the camera's view at a 90° angle from the top of the channel. The half-hall flowmeter was connected to an Arduino Uno through a digital pin. The Arduino program then counted the amount of raising peaks from the magnetic sensors over a 1-second period. This was converted to a flowrate (L/min) value by multiplying by 60 and a constant supplied by the manufacturer for calculating flowrate with magnetic peaks. This process repeated continuously throughout the experimentation period to designate a flow speed for each second of a test. The calculation was then passed over the serial cable to Tera-term where date and time could be recorded along

with flow speed. These values were synced with the date and time of the computer that stored the data and the camera time, so that it could be correlated to the exact time that video data was collected. The last step before starting the flow in the flume was to turn on the camera and reconfirm the set focal point in the center of the flume channel. Once each of these steps were completed, the experiment was ready to begin. Following the initial preparations, the flow in the channel was slowly increased to the first flow speed interval (~1 cm s^{-1}), which was sustained for ~20 seconds. Subsequently, the flow was increased by ~1 cm s^{-1} to the next flow speed interval and the process was repeated until flow speeds reached ~20 cm s^{-1}. Flow speed intervals included 1.1, 2.3, 3.4, 4.6, 5.7, 6.9, 8.0, 9.1, 10.3, 11.4, 12.6, 13.7, 14.9, 16.0, 17.1, 18.3, and 19.4 cm s^{-1}. Shear stress was calculated for these flow speeds using the quadratic stress law (Ross et al., 2009):

$$\tau = \rho * C_D * u^2, \quad (1)$$

where ρ is the density of seawater, u is the near bottom free-stream velocity, and CD is the drag coefficient ($2.5*10^{-3}$; Ross et al., 2009). Not all experiments reached the highest flow speed interval because a large number of particles were present in the flume at the higher intervals, no longer allowing individual particle recognition in the image processing. These speed intervals mimic the natural environment of the deep Gulf and can cause resuspension of sediment resulting in the formation of benthic nepheloid layers (Diercks et al., 2018).

1.4 Image Processing

Upon completion of core erosion experiments, individual image files were extracted from the video files for analysis. Using Windows Powershell©, an ffmpeg processing script, found in Appendix A, was used to extract four images per second from

each video file. Images were saved in tagged image file (TIF) format to ensure pixels were not distorted during image extraction. All image files from each video were then analyzed for particle number and size characteristics using Image Pro Plus®. Size characteristics gathered from Image Pro Plus® included individual particle area as well as maximum and minimum diameter and radius values for each particle. Images from each file were analyzed in chronological order so that sediment statistics from each image could be correlated with flow speed data. Prior to the counting process, the images were converted into grey scale data (0-65,565 pixel values) to normalize the images and to allow for a uniform analysis of each image given a specific pixel range to be counted as particles by the program. To be able to analyze moving particles within the video frame, a background subtraction process was conducted on each image (**Figure 2.4** (a-e)). This involved the program using the image directly before the image under analysis and taking out all features that existed in the same locations in both images. This process removed all pixels of the same value within both images so that any object that may not be related to the actual erosion and transportation of the sediment cores is not processed. Once the previous image was subtracted, the program counted objects of a certain pixel value range. A pixel value range was manually set to count only the particles that had entered the camera frame and particles that had been transported within the viewing area from one frame to the next. **Figure 2.4** (a-e) depicts the image processing procedure that was operated on each extracted frame of every video from the flume experiments. Particle characteristics collected from this process were initially saved as ASCII (extension CNT) files which were then converted to an excel friendly summary format by a binning software created by Roy Jarnagin. This program binned particles in ten 0.2 mm size

fractions and accumulated the particle size characteristics in each bin for each image for more efficient analysis of the particle statistics.

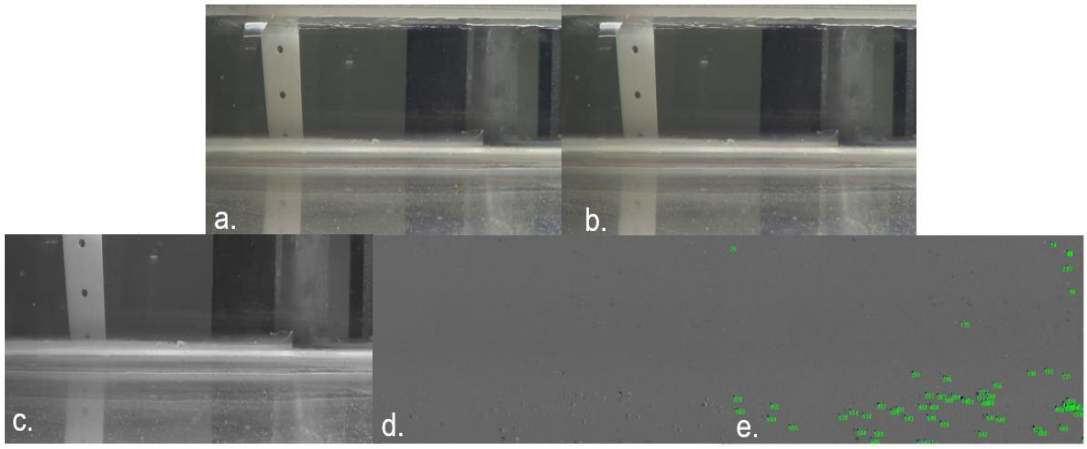

Figure 1.4 *Image Processing Procedure*

The set of images represent the image processing steps to gather particle data from videos of erosion experiments. (a) Image extracted from recorded video of an erosion experiment. (b) Image immediately following image a from the same erosion experiment. (c) Conversion of image to gray scale to allow for Image Pro® to assess a smaller color pixel value range. This is only shown for 1 image but what done for each image throughout the processing. (d) This image shows the background subtraction of image a from image b. This removes all static objects in the camera's view so that only moving particles are present in the image. (e) Result of counting procedure that highlights objects in pixel value range.

1.5 Particle Characteristics and Calculations

The data collected by the Image Pro Plus® processing script collected individual particle dimensions including diameter, roundness, short and long axis length, and area. These values for eroded sediment volume were then calculated by using

$$V=\pi a^2 b \text{ where,} \quad (2)$$

where a is the radius of short-axis and b is the radius of the long-axis. This formula was used because organic sediments in the surface layer, such as marine snow particles, are commonly known to lack perfect spherical shape. The volume formula is for an ellipsoid and a more accurate calculation for less spherical objects. Volume was calculated for

each particle in each frame throughout each experiment in attempt to identify trends in erosion timing and scale. Volume calculations were only completed on particles with radius values >0.2 mm, all particles below this value did not have a calculable volume within Image Pro®. Total volume values and average particle area values were calculated excluding the 0.0-0.2 mm size fraction. This decision was made due to particle counts being present in this fraction without flow within the channel on multiple occasions, resulting in a lack of confidence in the accuracy of the data in this size fraction. This could potentially be contributed to minor camera movements due to vibration of the frame on which the flume and camera were mounted or other unknown factors. This makes volume and particle size values only include the fine sand size fraction and larger, excluding clay and silt sized fractions. While it is acknowledged that mud sized particle typically dominate GoM sediments (Ward, 2017), unconsolidated surface sediments are likely organic rich particles that may be connected with mucus-like substances or other binding material, resulting in larger, more cohesive particles than the underlying sediment. Ignoring the mud fraction still allows for analysis of these larger particles, which is the primary focus of this research. In order to classify the sedimentation environment at coring location by the results of the flume experiments, an analysis of eroded sediment volume per flow speed interval was completed. The total sediment volume and particle size were calculated in each interval to see how these values would change with increasing flow speeds. Based upon the timing of initial sediment erosion and eroded volume peaks, sites were then classified as depositional or erosional, which are listed in **Table 3.1**.

1.6 Surface Sediment Properties

Multi-cores from the same sites used for flume analyses were analyzed by Dr. Gregg Brooks, Dr. Rebekka Larson of Eckerd College and Dr. Jeff Chanton at FSU. All three were part of the GOMRI funded project and agreed to provide their data for comparison with the erosion analyses. Several sediment properties including, mass accumulation rate (MAR) based on ^{210}Pb activity, bulk density (g/cm^3), percent carbon, and radiocarbon (Δ^{14}C) content, expressed in delta notation (‰) were determined. Cores were sampled following the procedures described in Schwing et al. (2017), which allow for sampling at millimeter scale resolution. Total Lead-210 ($^{210}Pb_{Tot}$) activity values were collected by gamma spectrometry on Series HPGe (High-Purity Germanium) Coaxial Planar Photon Detectors. Data were corrected for emission probability at the measured energy, counting time, sample mass, and converted to activity (disintegrations per minute per gram, dpm/g), using the International Atomic Energy Association (IAEA) organic standard IAEA-447 for calibration (Kitto et al. 1991; Larson et al. 2018). The activities of the ^{214}Pb (295 keV), ^{214}Pb (351 keV), and ^{214}Bi (609 keV) were averaged as a proxy for the "supported" Lead-210 ($^{210}Pb_{Sup}$) that is produced in situ (Baskaran et al., 2014) (Smith et al., 2002; Swarzenski, 2014). The $^{210}Pb_{Sup}$ activity was subtracted from the $^{210}Pb_{Tot}$ activity to calculate the "unsupported" or "excess" Lead-210 ($^{210}Pb_{xs}$), which is used for dating within the last ~100 years.

The Constant Rate of Supply (CRS) algorithm was employed to assign specific ages to sedimentary intervals within the $^{210}Pb_{xs}$ profile. The CRS algorithm is appropriate under conditions of varying accumulation rates (Appleby and Oldfieldz, 1983; Binford, 1990). Mass accumulation rates (MAR) were calculated for each data

point (i.e., “date”), based upon the CRS model results. The use of MAR corrects for differential sediment compaction down core, thereby enabling a direct comparison of $^{210}Pb_{xs}$ accumulation rates throughout a core (i.e., over the last ~120 years). Mass accumulation rates were calculated as follows:

$$\text{MAR } (g/cm^2/yr) = \text{dry bulk density} \quad X \quad \text{Linear Accumulation Rate (LAR)} \qquad (3)$$

Where:

$$\text{dry bulk density } (g/cm^3) = \text{sample dry mass } (g) \div \text{sample volume } (cm^3) \qquad (4)$$

$$\text{LAR} = \text{linear accumulation rate } (cm/yr) \qquad (5)$$

Bulk density (g/cm^3) was determined after extrusion of samples. Each sample was freeze-dried and weighted for dry mass to calculate bulk density (Binford, 1990; Appleby, 2001). Stable carbon (%C) was measured using a Carlo-Erba elemental analyzer coupled to an isotope ratio mass spectrometer at the University of Maryland Center for Environmental Science Chesapeake Biological Laboratory. The ^{14}C blanks were generally between 1.2 and 5 micrograms of C, producing a negligible effect on samples, which were over 1200 micrograms of C. The analysis of 22 replicate sediment samples yielded an average analytical reproducibility of ± 6.8‰ for $\Delta^{14}C$ and 0.2‰ for $\delta^{13}C$. Forty coal samples, representing fossil ^{14}C dead carbon, were analyzed to access the procedural blank of combustion, graphitization, and target preparation, over the course of this study. The average $\Delta^{14}C$ value was -995 ± 7‰. Additionally, 25-azalea leaf standards collected in Tallahassee, Florida in 2013 were analyzed; the average $\Delta^{14}C$ value was 31 ± 8‰.

- Results

Flow speed of initial sediment erosion, total sediment volume eroded, average particle size, and eroded flow speed of first peak in eroded sediment volume for each experiment are listed in **table 3.1**. Ancillary data of bulk density, average ^{210}Pb-based MAR (2014-2018), Δ^{14}C content and %C are also listed in **table 3.1**. The flow speeds at which particles were initially eroded and transported into the frame of the camera were recorded for each experiment. The flow speed was then used to calculate shear stress which ranged from 0.003 dyne cm^{-2} to 0.964 dyne cm^{2}. Flow speed and shear stress values will stated together throughout the discussion. Sediment from eight cores began to erode at flow speeds <2.0 cm s^{-1} (0.003 dyne^{-2}) and an additional seven cores began to erode <2.5 cm s^{-1} (0.013 dyne cm^{-2}). Total sediment volume eroded throughout each individual experiment was normalized to a value of 309 seconds, which was the average total experiment time of all cores. The normalization formula is

$$\text{Normalized Volume} = (309/x)*y, \quad (6)$$

where x is the total time of the experiment (s) and y is the total eroded volume (cm^3). The normalized total volume ranged from 4.5 cm^3 to 532.6 cm^3, with 66.8±110.6 cm^3 being the mean and standard deviation. Average particle area ranged from 0.38 mm^2 to 0.63 mm^2 with a mean of 0.45±0.05 mm^2. Eroded sediment volume peaks were chosen by analyzing curves of average eroded sediment volume per increasing flow speed interval. A value was considered a peak if there was an increase in sediment volume in the channel that increased during one flow speed interval above 1 cm^3 and then decreased in the next interval by 20% or more of the previous volume. The occurrences of this peak ranged in flow speeds from 5.7 cm s^{-1} (0.084 dyne cm^{-2}) to 16.0 cm s^{-1} (0.656 dyne cm^{-2}). Some

cores exhibited multiple peaks throughout experimentation, while others would not have the occurrence of a peak until the highest flow speed interval. The sediment volume eroded before the presence of the first peak was calculated and ranged from 0.0 – 43.7 cm^3 with a mean of 8.6 ±10.5 cm^3. Bulk density values from the upper 2 mm of sediment in each core had a mean of 0.20±0.08 g/cm^3. Percent carbon values, also taken from the upper 2 mm, had a mean of 1.92±0.57. Average MAR from years 2014-2018 ranged from 0.016 to 0.139 g cm^{-2} yr^{-1} with a mean of 0.06±0.036 g cm^2 yr^{-1}. Radiocarbon content was analyzed for the upper 2 mm of sediment and the values ranged from -139 ‰ to -319 ‰.

Station	Shear Stress of Initial Erosion (dyne cm^{-2})	Total Volume Eroded* (cm^3)	Average Particle Size (mm^2)	Shear Stress of First Peak in Sediment Volume (dyne cm^{-2})	Volume Eroded Before 1st Peak* (cm^3)	Bulk Density (g cm^{-3})	% Carbon	Average MAR 2014-2018 (g cm^{-2} yr^{-1})	Surface $\Delta^{14}C$ (‰)	Post-Cruise Flume Experiment Classification
PS1825-MC04	0.053	30.7	0.45	0.482	9.3	0.12	2.13	0.057	-194.40	Erosional
PS1825-MC05	0.003	21.4	0.63	0.164	3.4	0.16	2.25	0.035	-177.30	Depositional
PS1825-MC06	0.053	73.27	0.51	0.656	39.8	0.27	2.37	0.016	-180.20	Erosional
PS1825-MC07	0.003	37.2	0.45	0.335	3.5	0.18	2.6	0.047	-181.40	Depositional
PS1825-MC08	0.03	13.8	0.45	0.566	7.9	0.18	1.48	0.062	-238.70	Erosional
PS1825-MC09	0.03	4.6	0.39	0.084	0.1	0.18	1.45	0.118	-314.80	Erosional
PS1825-MC10	0.013	22.1	0.39	0.121	0.1	0.18	1.29	0.076	-233.10	Erosional
PS1825-MC11	0.013	532.6	0.49	0.053	0.1	0.21	1.40	0.053	-243.80	Depositional
PS1825-MC12	0.03	31.5	0.46	0.164	0.1	0.15	2.46	0.021	-201.40	Erosional
PS1825-MC13	0.013	30.9	0.50	0.482	12.9	0.32	2.13	0.028	-165.00	Erosional
PS1825-MC14	0.003	211.9	0.47	0.121	7.5	0.12	2.92	0.014	-139.90	Depositional
PS1825-MC15	0.013	81.2	0.44	0.405	11.4	0.10	2.84	0.040	-207.90	Erosional
PS1825-MC16	0.013	57.2	0.46	0.271	1.8	0.38	1.63	0.139	-319.30	Depositional
PS1825-MC17A	0.003	25.4	0.42	0.121	0.1	0.24	1.80	0.058	-227.10	Depositional
PS1825-MC17B	0.013	30.1	0.46	0.335	2.8	0.24	1.80	0.058	-227.10	Depositional
PS1825-MC18	0.013	4.5	0.43	0.214	0.1	0.21	1.35	0.134	-255.20	Erosional
PS1825-MC19	0.003	29.7	0.40	0.271	4.5	0.16	1.32	0.090	-225.20	Depositional
PS1825-MC20	0.003	50.0	0.44	0.121	0.8	0.29	1.40	0.060	-258.90	Depositional
PS1825-MC21	0.053	22.8	0.42	0.656	4.9	0.25	1.51	0.032	-186.60	Erosional
PS1825-MC22	0.053	38.3	0.38	0.566	7.7	0.22	-	-	-	Erosional
PS1825-MC23	0.003	76.9	0.45	0.482	12.7	0.04	-	-	-	Erosional
PS1825-MC30	0.03	99.8	0.46	0.405	21.2	0.12	2.72	0.019	-167.00	Depositional
PS1825-MC31-DWH01	0.003	18.0	0.42	0.405	4.2	0.27	1.46	0.053	-211.20	Erosional

Table 2.1 Flume Erosion Data with Other Sedimentary Characteristics of the Upper 2 mm.

Table showing data collected from sediment flume erosion experiments and surface sediment sampling. *Indicates the total volume was normalized to 309 seconds, which was the mean experiment time for all cores

2.2 Environment Classification by Eroded Volume Curves

A reanalysis of sedimentary environment from pre-cruise classification was done on coring locations based upon results of resuspension flume experiments. Graphs were created for each experiment that contained normalized eroded volume per interval, normalized particle counts per interval, and average particle size eroded per each flow speed interval. Error bars were not plotted with the average particle area values due to most cores having all error bars overlap in each interval. Eroded sediment volume and particle counts were normalized to 20 second intervals so that each experiment could be analyzed on the same period per interval. The normalization process for each interval was the same as the normalization process for the total eroded volume but using 20 seconds as the total time and using the volume eroded in the interval being analyzed instead of the total volume. An example of an erosion graph that was classified as a depositional environment is shown in **Figure 3.1** (a). Particles began to erode at 1.1 cm s^{-1} (0.003 dyne cm^{-2}) with the average volume being near 0 mm^3 value. Particles were present in each interval for the entire experiment with low volumes until the 4.6 cm s^{-1} interval. A peak in normalized sediment volume was observed at the 6.9 cm s^{-1} (0.121 dyne cm^{-2}) flow interval of 0.27 cm^3. Eroded sediment volume and particle area decreased over the next three flow speed intervals that range from 8-10 cm s^{-1}. Eroded volume and particle area increased again at the 11.4 cm s^{-1} (0.482 dyne cm^{-2}) flow speed interval and increased at each interval for the rest of the experiment. Cores with graphs that mimic a similar pattern were also considered depositional locations.

Graphs that are considered to represent erosional environments show different characteristics. **Figure 3.1** (b) presents an example of an erosional environment. Particles

were not present in the flume until a flow speed of 3.4 cm s^{-1} (0.03 dyne cm^{-2}) was reached. At this speed, an average volume near 0 mm^3 with an average particle area of 0.35±0.11 mm^2 were eroded . The average eroded volume did not exceed 0.01 cm^3 until the flow speed reached 11.4 cm s^{-1} (0.335 dyne cm^{-2}), though there was a small peak in particle area of 0.53±0.31 mm^2 at the 5.7 cm s^{-1} flow speed. There was no peak present in the data until the 14.9 cm s^{-1} (0.566 dyne cm^{-2}) flow interval that had 0.26 cm^3 eroded sediment volume. All sites were classified as either erosional or depositional based on their curves, which are all shown in Appendix B.

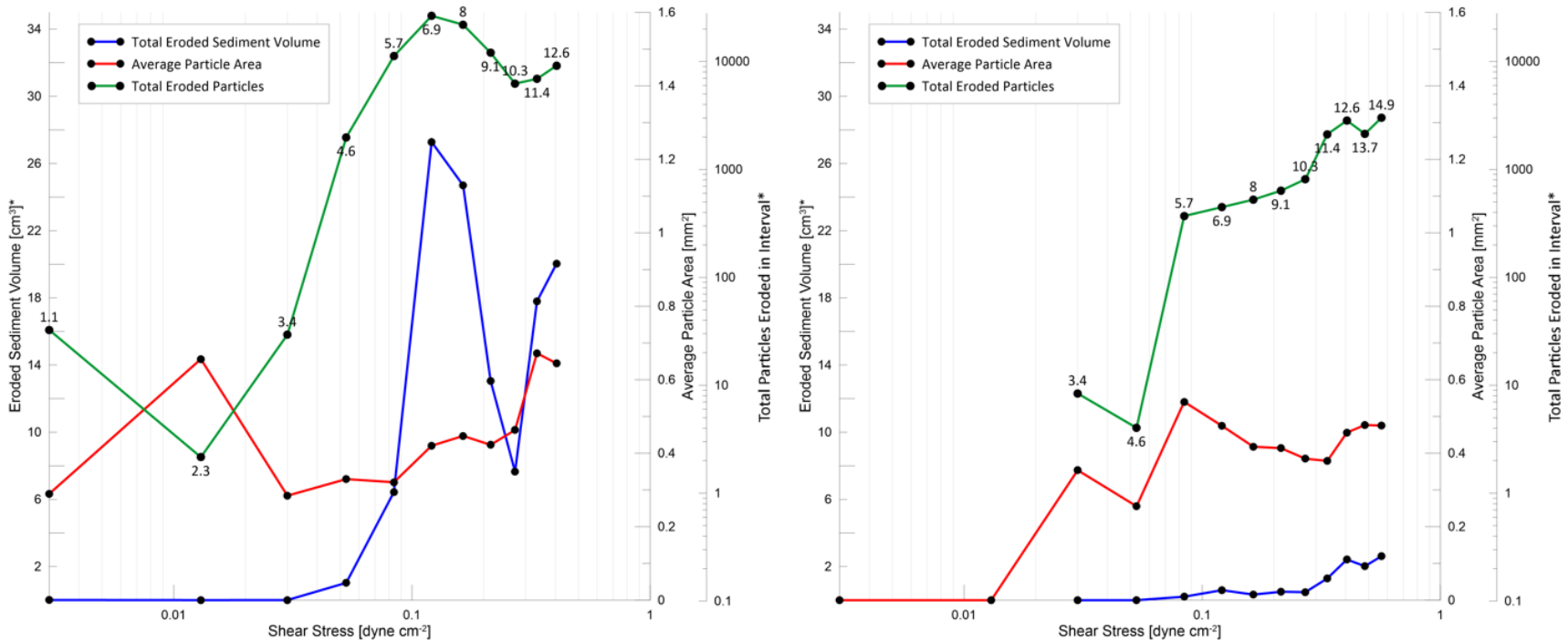

Figure 2.1 *Example of Sediment Erosion Curves*

Data points plotted in figure are sediment volume and particle counts per interval, normalized to 20 seconds, and average particle area per interval. These values were also calculated without the 0.0-0.2 mm size fraction as in earlier calculations. The red line is plotting average particle area (mm^2), the blue line shows normalized sediment volume (cm^3), and the green line shows normalized particle counts. Values listed on the particle counts line are flow speed values for each interval. (A) shows an example of a depositional volume curve due to the early onset of large particles, low speed of initial erosion, and low flow speed of first peak. (B) shows an example of an erosional volume curve due to low volume at low flow speed and the late presence of a sediment volume peak. *Represents the data present is normalized to 20 seconds

2.3 Correlation of Surface Sediment Characteristics and Erosion Data

To determine if there is a relationship between the flume erosion experiments and the surface sediment characteristics, a correlation scatterplot matrix was created comparing each of the data categories in **Table 3.1**. **Figure 3.2** shows the plots and correlations of each component. The relationships with the largest absolute correlation coefficients were between surface MAR and $\Delta\ ^{14}C$ (-0.87), flow speed of first peak and sediment volume eroded before first peak (0.71), MAR and percent carbon (-0.66), and $\Delta^{14}C$ and percent carbon (0.69). Each of these relationships had an absolute correlation coefficient greater than ±0.50. Other, less correlated, relationships were present between sediment volume eroded before first peak and MAR (-0.49), sediment volume eroded before first peak and percent carbon (0.47) sediment volume eroded before first peak and $\Delta\ ^{14}C$ (0.46), flow speed of first peak and $\Delta\ ^{14}C$ (0.45), bulk density and percent carbon(-0.44) and flow speed of first peak and flow speed of initial erosion (0.43). All other relationships had absolute correlation coefficient less that ±0.40.

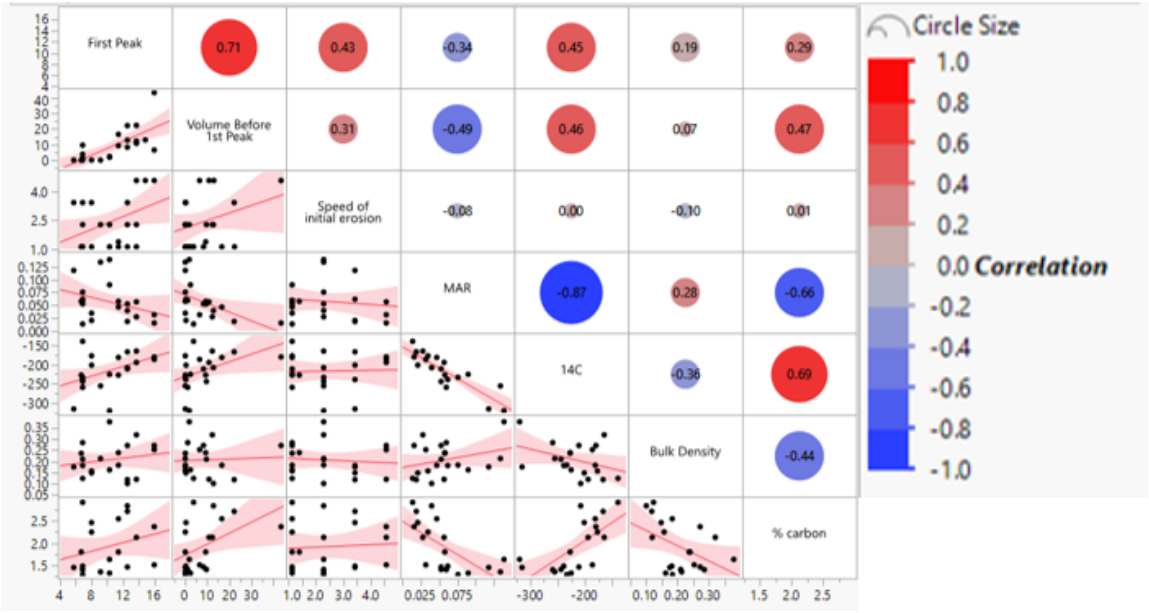

Figure 2.2 *Scatterplot Matrix of Values from Table 3.1*

This figure shows correlations between each value listed in table 3.1. Correlation values are plotted as well to show relationship between different aspects of erosion experiments and surface sediment characteristics.

3.1 Sedimentation Regions

Based on variations in sedimentary characteristics and flume data, Diercks et al. (in revision) presented three geographic Regions in the study area. The following discussion will adhere to their characterization of the sedimentation within the study area and discuss the flume analyses data in reference to these three Regions.

Region 1 included cores 4 and DwH 01;

Region 2 SE of Region 1, includes cores 5, 6, 12, 13, 14, and 30;

Region 3, further to the SE in the study area, included sites 7, 8, 9, 10, 11, 15, 16, 17A & B, 18, 19, 20, 21, 22, and 23.

Discussed in detail in Diercks et al. (in revision), cores in all three Regions contained thin, mm-scale, sub-parallel laminae and wavy bed units that are characteristic of sediment re-deposition by gravitational processes. Inclined beds and color-banded units were only present in cores from Regions 2 and 3, which are indicative of low density, fine-grained turbidity currents, slide, or slumps (Coleman et al., 1986; Brooks et al., 2015). **Figure 4.1** shows the spatial trends in flow speed of first peak values, $\Delta^{14}C$ concentrations, and %C throughout the study area with lines dividing the area into the three regions.

Region 1

Region 1 received the highest inputs of contaminated sediments in the short-term following the DwH oil spill (Chanton et al., 2012; Passow et al., 2012; Brooks et al., 2015; Yan et al., 2016; Ziervogel et al., 2016; Romero et al., 2017). This Region has the highest potential for downslope transport due to the high slope angles present as well as

the varying seafloor morphology. The two cores in this Region, DwH01 and 04, had their first peak in eroded sediment volume occurring at 0.405 dyne cm^{-2} (12.6 cm s^{-1}) and 0.482 (13.7 cm s^{-1}) respectively, which was above average for this study and suggests the lack of easily resuspended material in the surface layer (**Table 3.1**). In core 4, initial sediment erosion began at 0.053 dyne cm^{-2} (4.57 cm s^{-1}), which was the highest shear stress needed to begin erosion. With only two cores present in this Region, it is hard to make a designation on erosional characteristics for the entire Region. Diercks et al. (in revision) completed a deeper analysis into the sedimentology and chemistry of sites 4 and DwH 01 as well as 3 additional cores in this Region. The three additional cores were unable to be analyzed in the resuspension flume due to damage to the cores during transit. Diercks et al. (in revision) concluded that this Region showed the presence of episodic sediment accumulation and has potential for longer-term accumulation of redistributed sediments from up-slope areas. The cores in this Region had differing sedimentological data with site 04 having above average %C (2.13) and younger $\Delta\ ^{14}C$ (-194.4‰) values, while site DwH01 had low %C (1.46) and older $\Delta\ ^{14}C$ (-211.2‰) values. Even with these differences, the erosion of these cores exhibited similar attributes. Both sites had below average total eroded volume, at or below average particle area, and volume peaks occurring at above average shear stresses for the study. The combination of these factors suggest the lack of an easily resuspendable surface layer and high-energy events are required to transport large volumes of sediment from this Region.

Region 2

Region 2 contains a similar bathymetry as Region 1 in the most NW portion of the study area, but transitions to an open plain setting with very subtle slopes in the SE

portion. The sites in this Region contained the highest %C values in the study as well the most enriched $\Delta\ ^{14}C$ values, which is indicative of material being sourced from the sea surface and not from resuspension (Chanton et al., 2018). Previous studies have noted sediment resuspension in this area triggered by near inertial currents and other tropical storm induced events, which may restrict long-term sediment deposition associated with gravitational down-slope transport, resulting in resuspended material potentially bypassing this Region or only residing for a short time (Gardner and Sullivan, 1981; Isley et al., 1990; Diercks et al., 2018).

Cores 6, 13, and 30 exhibited their first eroded sediment volume when shear stress reached >0.164 dyne cm^{-2}, suggesting the lack of an easily resuspendable surface layer. Sediment erosion in core 14 peaked at 0.121 dyne cm^{-2} (6.9 cm s^{-1}), but this core was the most northern site in the study area and may be an outlier for the Region. There was not a noticeable difference in the shear stress of initial erosion compared to the other Regions, as cores in this Region had resuspension occur at the lowest (0.003 dyne cm^{-2}) and highest (0.053 dyne cm^{-2}) shear stresses observed. Cores 5, 6, and 13 had the largest average eroded particle size in the study, and all other cores in the Region were above average in eroded particle size. This is likely attributed to the high %C facilitating the formation of large aggregates. In reviewing GoPro videos of the cores surface, the cores from this Region appeared to have dark, organic rich large aggregates. A noteworthy process recognized during the experiments was the hydrodynamic behavior of aggregates as a function of core morphology as they were initially eroded. Videos showed multiple occurrences of aggregates on the upstream side of the core being transported down-channel to the lee side of the cores where they were trapped until higher flow speeds

transported them into the frame of the camera used for particle counting. This could explain why some of the experiments on cores in this Region did not present a peak in large particle sizes early on in the experiment, but only at higher flow speeds. Cores 5, 12, 13, and 30 had a larger average particle size in the 2nd half of their respective experiments, revealing this delay in aggregate transport into the cameras field of view. With cores 6, 14, and 30 having 3 of the top 6 highest total volumes eroded, sites in this Region have the potential to have large amounts of sediment transported to other areas, but it would require high-energy events.

Region 3

The sites in Region 3 were located in the greatest water depths (>2000 m) in this study and low slope angles (<2°) trending from the NW to SE. Region 3 had the highest MAR values and strong predominance of episodic sediment accumulation identified in the sedimentary record (Personal conversation: Gregg Brooks and Bekka Larson), which may be indicative of reoccurring down-slope transport events being delivered into the Region. Low %C and depleted $\Delta\ ^{14}C$ values in this Region suggest the sediment present in this Region is older, reworked material being deposited from upslope (Diercks et al., 2018). Transport from upslope and deposition into this Region would result in a loosely consolidated surface layer of fine-grained sediments that would be easily resuspended at low flow speeds, producing a sediment particle size distribution towards the fine particles. The flume data defends this claim as this Region contains 6 cores (sites 9, 10,11, 17A, 18, and 20) that had a peak in eroded sediment volume occur at a shear stress of 0.256 dyne cm^{-2} (6.9 cm s^{-1}), as well as 5 cores (sites 7, 17A, 19, 20, and 23) showing initial resuspension of material occurring at the lowest possible flow speed. Average

particle size of eroded particles in this Region were consistently at or below average (0.45 mm^2), which may be associated with the low %C values also present. GoPro videos obtained during the flume analyses of cores in this Region show the visual difference in the surface material as the material appeared lighter in color and had smaller aggregates in comparison to the organic rich Region 2.

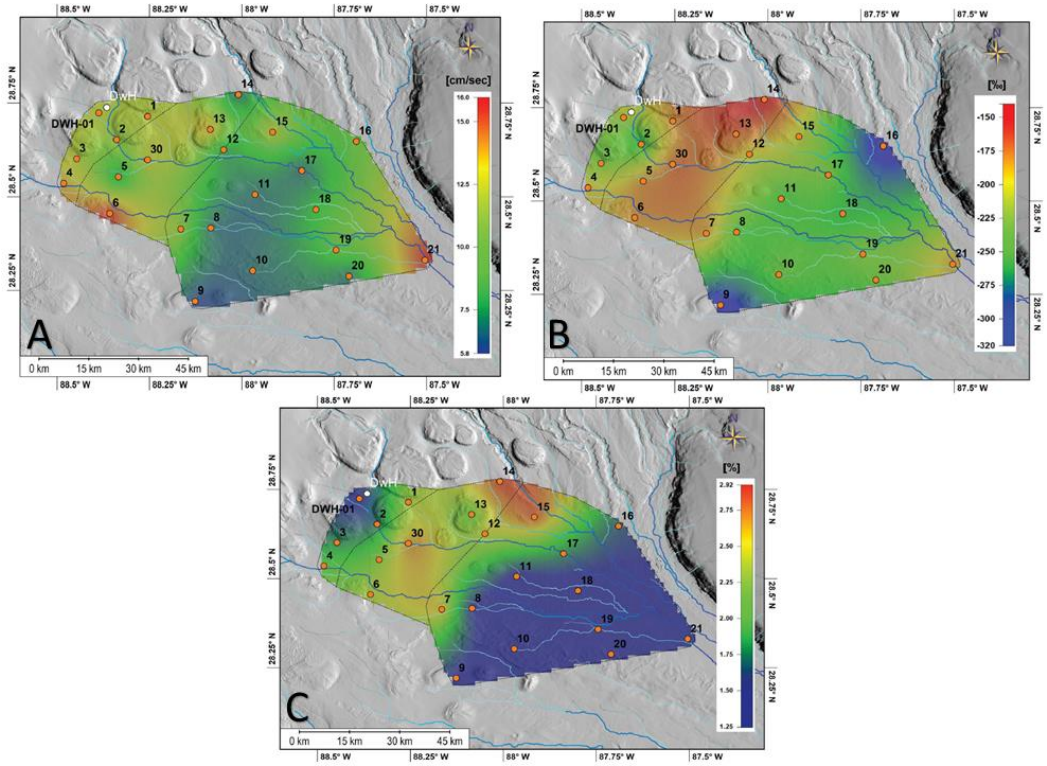

Figure 3.1 Heat Maps of Flow Speed of First Eroded Sediment Volume Peak (A) $\Delta^{14}C$ (B), and %C (C)

Heat maps overlying modelled drainage pathways with labelled coring sites and lines dividing the maps into the three discussed regions. (A) Shows the flow speed of first eroded sediment volume peaks (cm s^{-1}). (B) Shows $\Delta^{14}C$ (‰) values for the upper 0-2 mm intervals of each coring site. (C) Shows %C concentrations for the upper 0-2 mm interval of each sediment core.

3.2 Sedimentary Environment Reclassification

Sedimentary structures reflective of gravity driven sediment re-deposition were present in nearly all cores in the study area (Diercks et al., in revision). Thin, mm-scale, sub-parallel, wavy bed units, inclined beds and color-banded units are all commonly

occurring structures present in adjacent Mississippi Fan deposits that can be attributed to low-density, fine-grained turbidity current, and/or submarine slumps (Coleman et al., 1986; Vonk et al., 2015; Ward et al., 2017). Sites were reclassified from their original environment predictions based upon presence and timing of initial erosion and eroded sediment volume peaks. These original classifications were based on a morphological stream analysis performed during coring site selections prior to the research cruise actually collecting the cores. Cores that had initial sediment erosion beginning at $\leq$2.3 cm s^{-1} (0.013 dyne cm^{-2}) and exhibited a peak in eroded volume at $\leq$11.4 cm s^{-1} ($\leq$0.335 dyne cm^{-2}) were classified as depositional sites. If a core exhibited both of these characteristics, it suggested the surface material could be initially moved under low flow conditions and the material could be moved in large pulses under normal conditions for the GoM (Jochens and DiMarco, 2008; Ross et al., 2009; Diercks et al., 2018). For this study, sites 5, 7, 10, 11, 14, 16, 17, 19, and 20 met these stipulations. Site 18 also met these requirements but was not classified as a depocenter due to the low volume eroded throughout the experiment.

Region 1 contained no sites that were classified as depocenters. These sites were located in the shallowest Region of the study area. The seafloor in this region had the steepest slope gradients, where flow speed would be greatest, and likelihood of downslope transport by gravitational processes or shear stress triggered transport would be increased (Ross et al., 2009; Morey et al., 2020; Diercks et al., in revision). The cores from this region had nearly identical sediment volume curves with the volume peaks occurring at the 2nd highest shear stress in their respective experiment, suggesting

surface material in this region is lacking a defined fluffy layer and/or has resistant material due to increased %C concentrations.

In Region 2, sites 5 and 14 were classified as depositional. This Region had the highest %C concentrations throughout (>2.13%), which likely contributed to the increased shear stresses needed to eroded large amounts of surface material. Contrary to the other depositional sites, core 14 had the highest %C value in the entire study area and core 5 had above average %C, but still exhibited a large pulse of sediment occurring at <10cm s^{-1}. All other sites in this Region met the criteria of being erosional environments. Diercks et al., (in revision) cite $^{210}Pb_{xs}$ data that shows more consistent, stable accumulation of sediment matched with low MARs reflecting material from episodic down-slope transportation is not accumulating here.

Region 3 contained the majority of the sites classified as depocenters in this study: 7, 10, 11, 16, 17, 19, and 20. As stated above, this is a gently sloping region in the greatest water depths of the study area. Sediment volume peaks occurred at lower bed shear stresses in this region, which suggests the presence of an easily resuspended surface layer. The measured low %C and depleted $\Delta\ ^{14}C$ values suggest the material in this Region could be rebound material that has been utilized during the transportation journey. This prolonged exposure to degradational processes during transportation results in the material being easier to resuspend once in contact with the seafloor as seen in other studies (Walsh et al., 1988; Gardner and Walsh 1990; Diercks et al., 2018).

3.3 Parameter Correlations

Correlations between flume data and surface sediment properties were analyzed for any noteworthy relationships related to the classification of sites. The flow speed of

the first peak of eroded sediment correlated best with $\Delta^{14}C$ (-0.45, n=21, p=0.13), showing that cores with younger surface material did not exhibit an eroded volume peak until higher shear stresses. Younger carbon compounds, potentially sourced from primary production, has the ability to act as a binding material for surface sediments, which may result in increased resistance to stress (Thomsen and Gust, 2000; Chanton et al., 2018). This relationship was present in the flume experimentation as cores with more enriched $\Delta^{14}C$ had eroded volume peaks occurring at higher flow speeds than cores with depleted $\Delta^{14}C$ values. Low-density turbidity flows, far field earthquakes, or slumps/slides are common to the GoM and present a potential delivery mechanism of depleted $\Delta^{14}C$ to the study area (Coleman et al., 1986; Fan et al., 2020). Sediment from cores that have undergone this transportation, would likely see decrease in carbon content as it is continually utilized during the journey. The lack of fresh carbon to bind the material can result in easier resuspension of surface material and presence of smaller particles, which can be seen in the flume data.

– Conclusions

All sites included in this study were depositional over the last ~100 years, but varied in surface sediment characteristics and scale of accumulation. The variance in these characteristics revealed a difference in resilience to shear stress in different regions of the study. Shear stress of initial erosion and eroded sediment volume peaks show the likelihood of material being preserved in a region or eroded and accumulating in different locations. All sites in the study had initial particle erosion begin ≤4.1 cm s^{-1} (τ=0.053 dyne cm^{-2}) suggesting small-scale movement of material occurs under low stress conditions in the northern GoM. Peaks in sediment erosion varied from region to region with Regions 1 and 2 requiring higher shear stress for an observed peak compared to Region 3. This trend may be a result of the age of the material, as cores in Regions 1 and 2 had younger material with higher %C concentrations in the uppermost layer of the sediment. Sites in Region 3 had more depleted $\Delta\ ^{14}C$ values and lower %C concentrations, which is indicative of degraded material being sourced from long-term transportation processes.

The hypothesized difference in eroded particle size did not appear related to the structural differences at the coring sites, but appeared to be more representative of the age of the material in the region. Sites in Regions 1 and 2 had a higher average eroded particle size (0.49 mm^2) than sites in Region 3 (0.43 mm^2). An interesting result in analyzing particle size differences was that particles from Regions 1 and 2 increased in size following an eroded volume peak, while particles from Region 3 decreased in size in most cases. This may be an artifact of the hydrodynamics occurring in the flume that caused some large aggregates to be trapped on the lee side of the sediment core until

higher flow speeds, or it could be a result of the larger, more organic rich particles in Regions 1 and 2 requiring elevated shear stress to erode the particles down-channel.

The result of this research shows evidence of older, rebound material being more easily resuspended and susceptible to downslope transport in GoM than newly deposited material. In combination with Diercks et al., (in revision), this evidence suggests that, over time, a larger area of the GoM than originally recognized has been impacted by the DwH oil spill by identifying areas that are potential receptors of DwH oil in deep waters SE of the wellhead.

APPENDIX A – Windows PowerShell Script

cd \

cd .\Users\

cd .\(\

cd .\Desktop\

cd .\MC17A\ (the core directory)

ffmpeg -i MC17A.mts -r 4 -pix_fmt rgba MC17A_%04d.

APPENDIX B Erosion Graphs

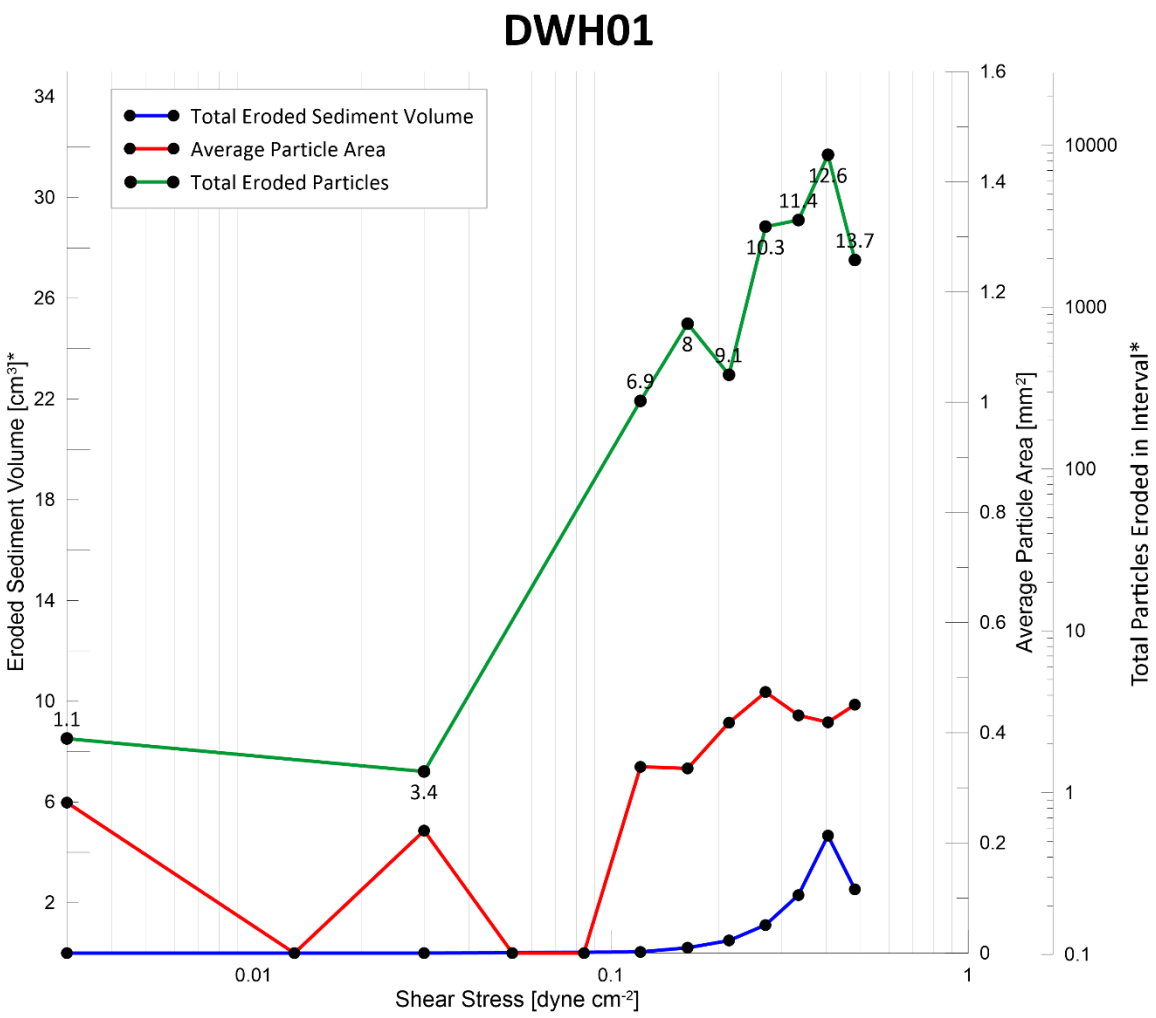

Figure B.1 *Erosion Graph of Core DWH01*

Data points plotted in figure are sediment volume and particle counts per interval, normalized to 20 seconds, and average particle area per interval. These values were also calculated without the 0.0-0.2 mm size fraction as in earlier calculations. The red line is plotting average particle area (mm^2), the blue line shows normalized sediment volume (cm^3), and the green line shows normalized particle counts. Values listed on the particle counts line are flow speed values for each interval.

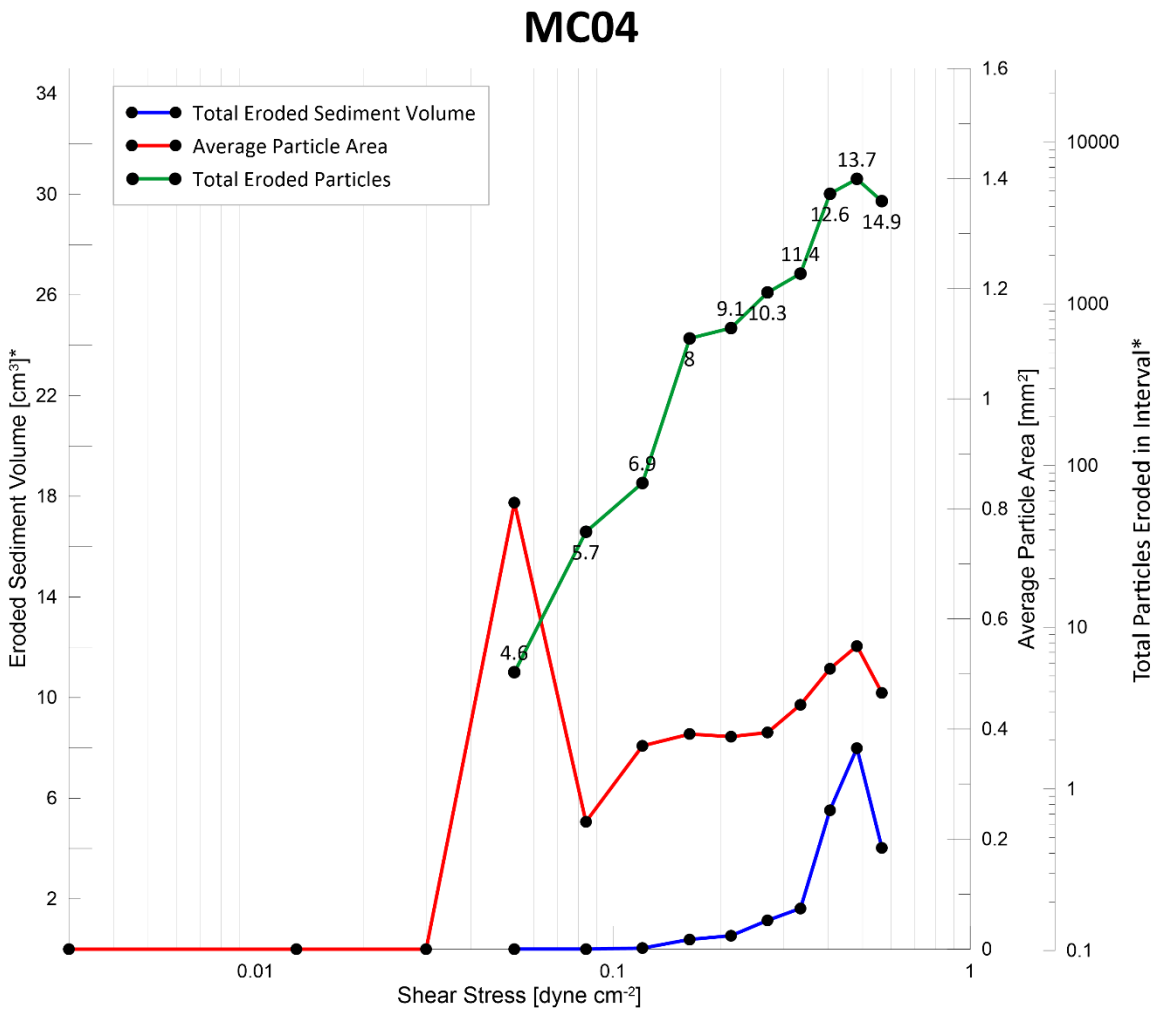

Figure B.2 *Erosion Graph of Core MC04*

Data points plotted in figure are sediment volume and particle counts per interval, normalized to 20 seconds, and average particle area per interval. These values were also calculated without the 0.0-0.2 mm size fraction as in earlier calculations. The red line is plotting average particle area (mm^2), the blue line shows normalized sediment volume (cm^3), and the green line shows normalized particle counts. Values listed on the particle counts line are flow speed values for each interval.

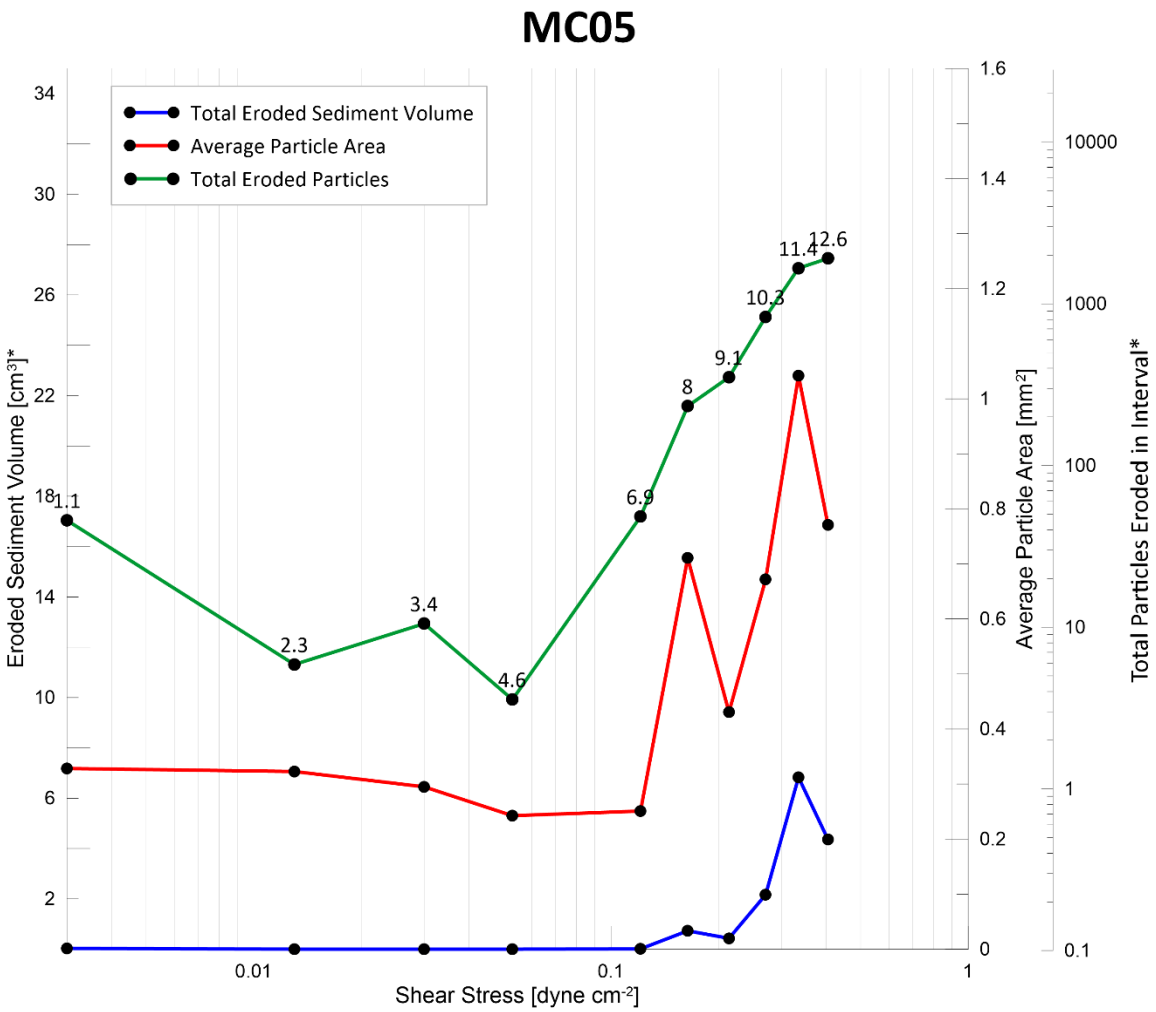

Figure B.3 *Erosion Graph of Core MC05*

Data points plotted in figure are sediment volume and particle counts per interval, normalized to 20 seconds, and average particle area per interval. These values were also calculated without the 0.0-0.2 mm size fraction as in earlier calculations. The red line is plotting average particle area (mm^2), the blue line shows normalized sediment volume (cm^3), and the green line shows normalized particle counts. Values listed on the particle counts line are flow speed values for each interval.

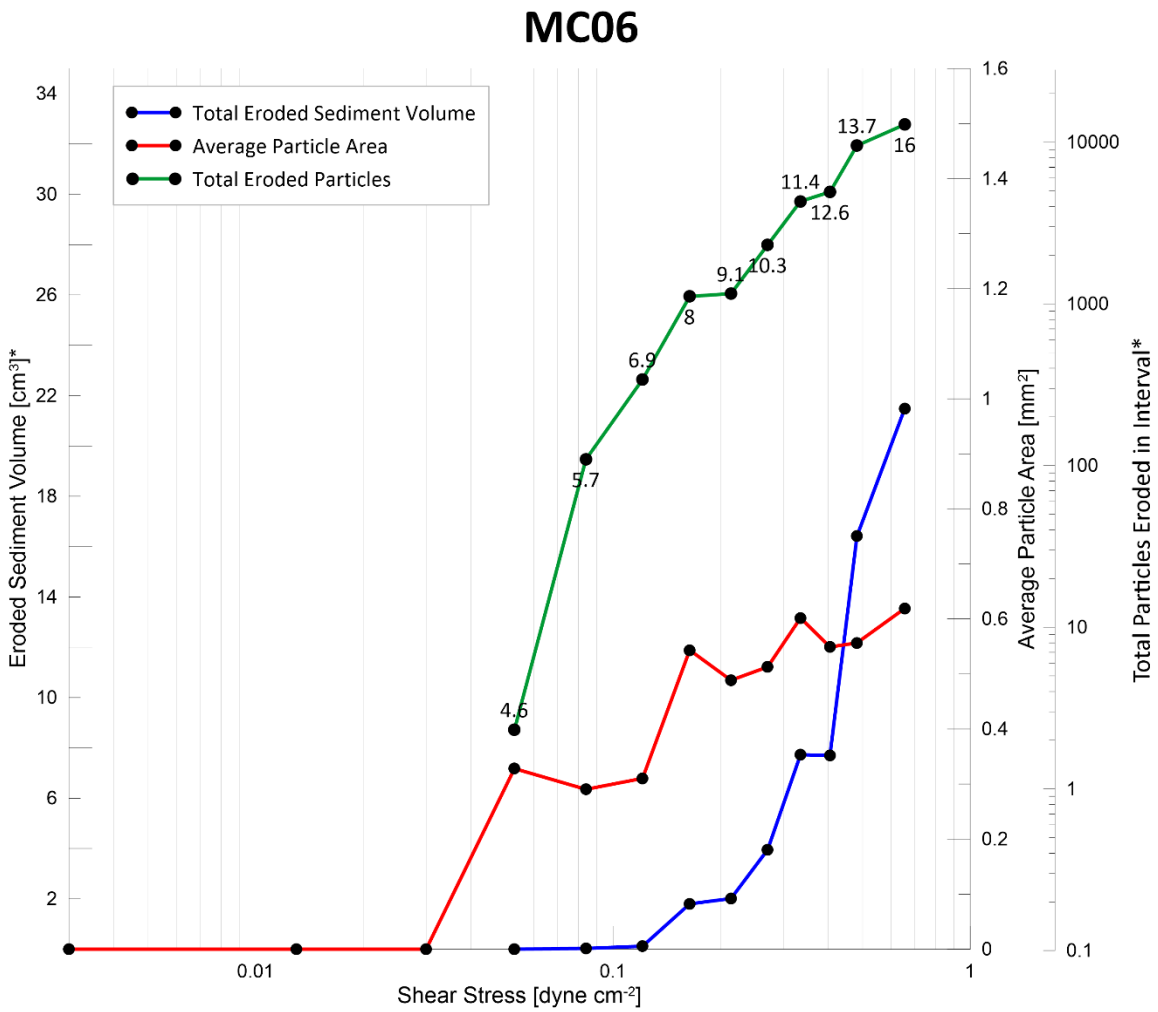

Figure B.4 *Erosion Graph of Core MC06*

Data points plotted in figure are sediment volume and particle counts per interval, normalized to 20 seconds, and average particle area per interval. These values were also calculated without the 0.0-0.2 mm size fraction as in earlier calculations. The red line is plotting average particle area (mm^2), the blue line shows normalized sediment volume (cm^3), and the green line shows normalized particle counts. Values listed on the particle counts line are flow speed values for each interval.

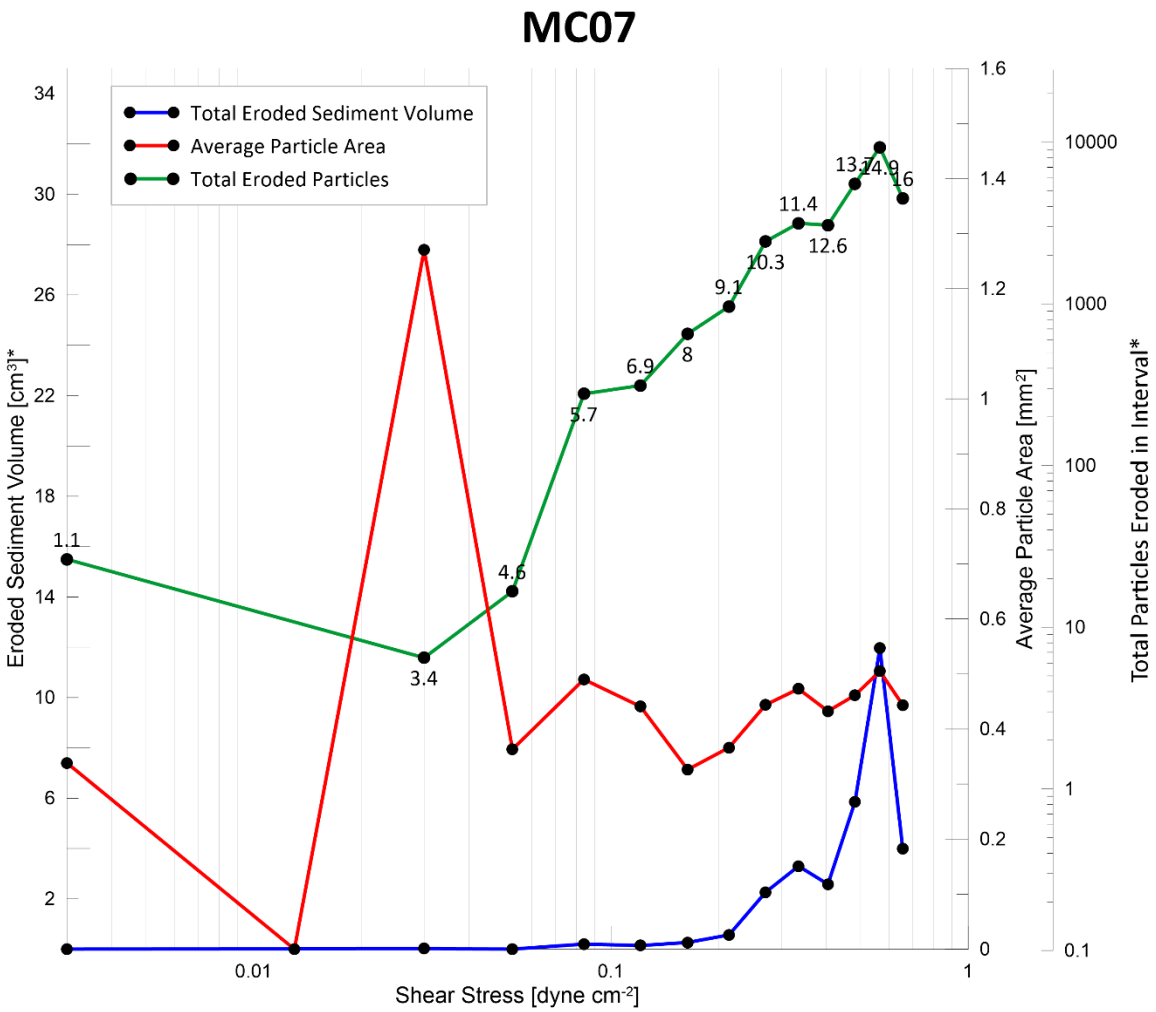

Figure B.5 *Erosion Graph of Core MC07*

Data points plotted in figure are sediment volume and particle counts per interval, normalized to 20 seconds, and average particle area per interval. These values were also calculated without the 0.0-0.2 mm size fraction as in earlier calculations. The red line is plotting average particle area (mm^2), the blue line shows normalized sediment volume (cm^3), and the green line shows normalized particle counts. Values listed on the particle counts line are flow speed values for each interval.

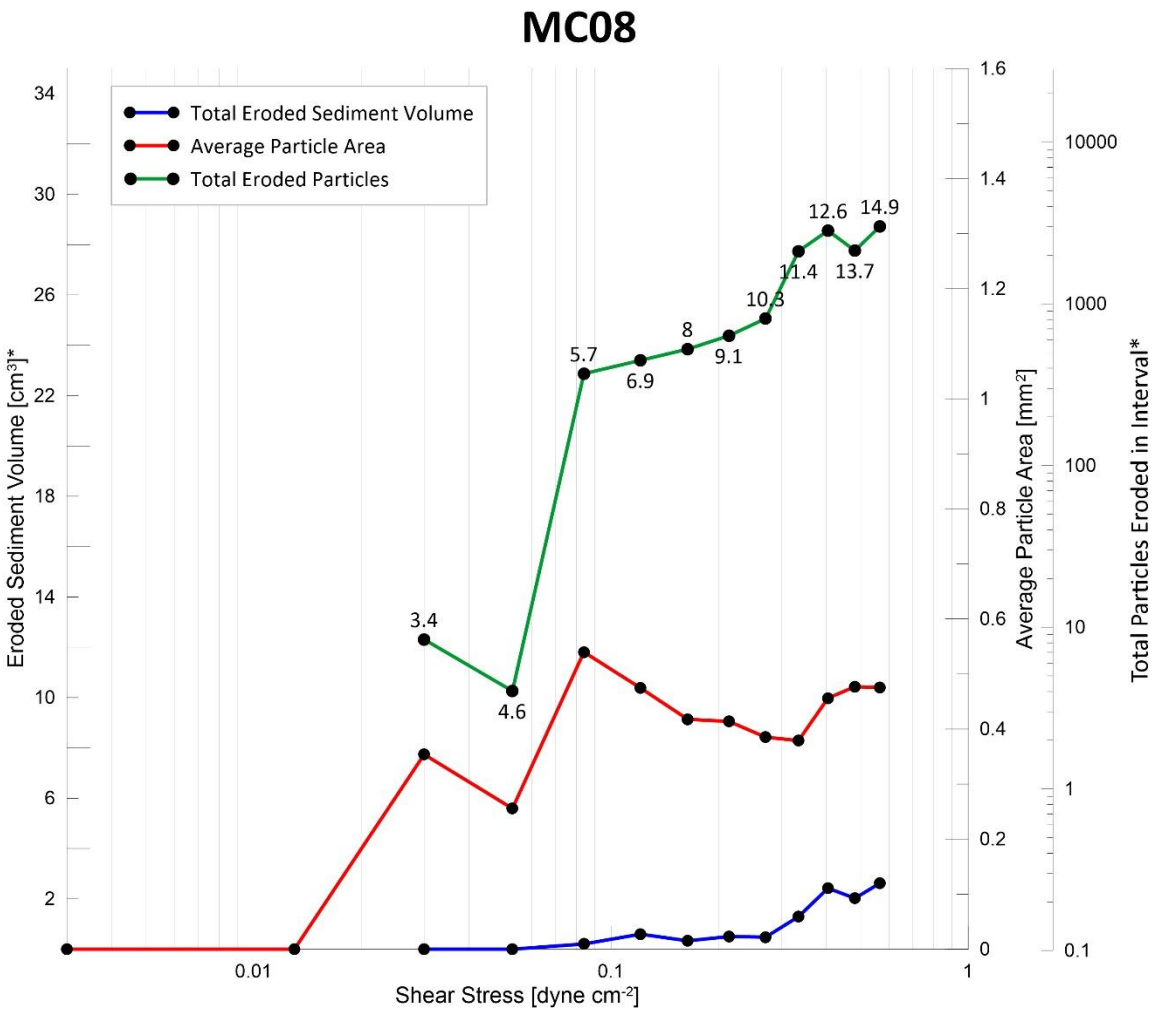

Figure B.6 *Erosion Graph of Core MC08*

Data points plotted in figure are sediment volume and particle counts per interval, normalized to 20 seconds, and average particle area per interval. These values were also calculated without the 0.0-0.2 mm size fraction as in earlier calculations. The red line is plotting average particle area (mm^2), the blue line shows normalized sediment volume (cm^3), and the green line shows normalized particle counts. Values listed on the particle counts line are flow speed values for each interval.

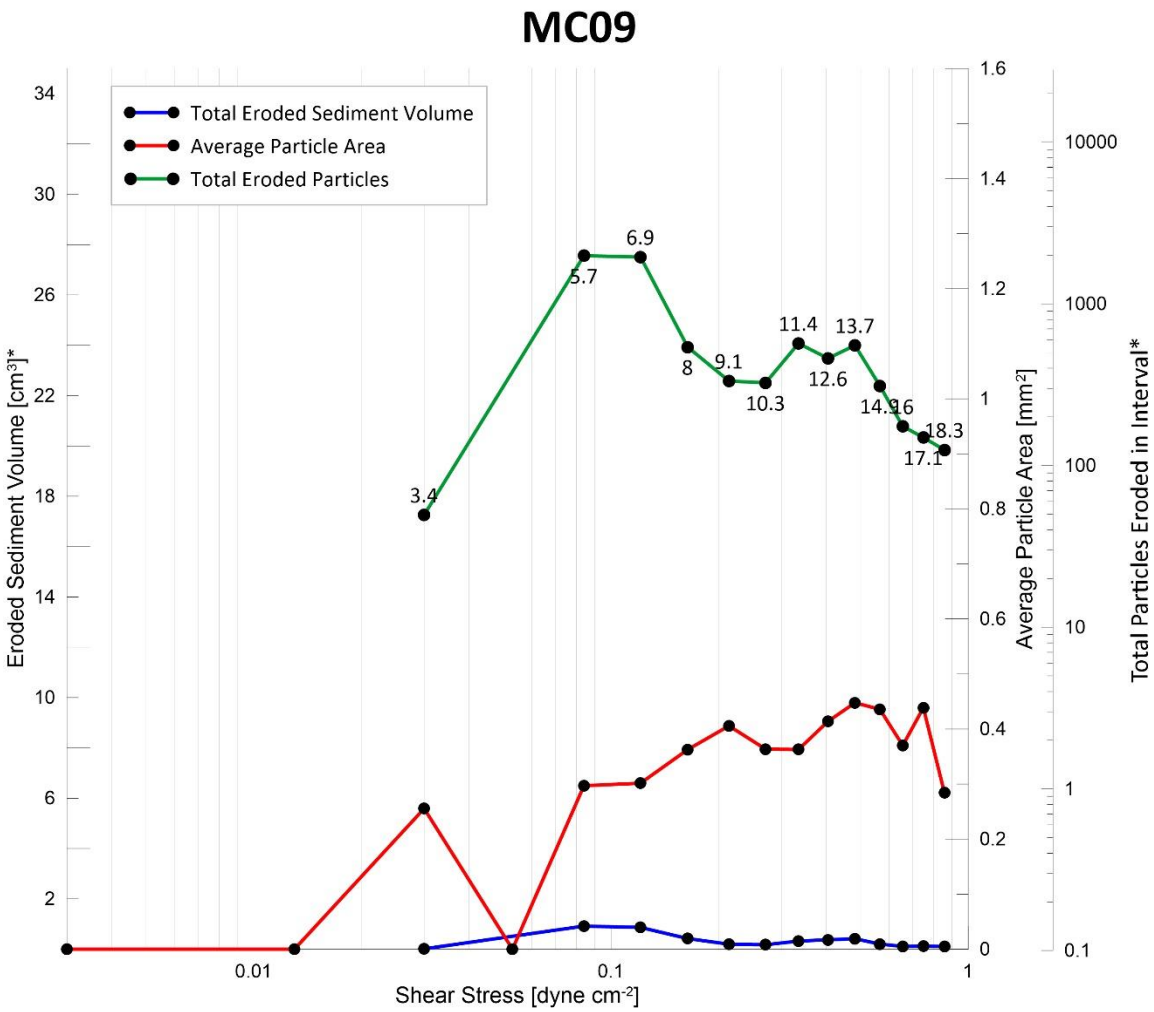

Figure B.7 *Erosion Graph of Core MC09*

Data points plotted in figure are sediment volume and particle counts per interval, normalized to 20 seconds, and average particle area per interval. These values were also calculated without the 0.0-0.2 mm size fraction as in earlier calculations. The red line is plotting average particle area (mm^2), the blue line shows normalized sediment volume (cm^3), and the green line shows normalized particle counts. Values listed on the particle counts line are flow speed values for each interval.

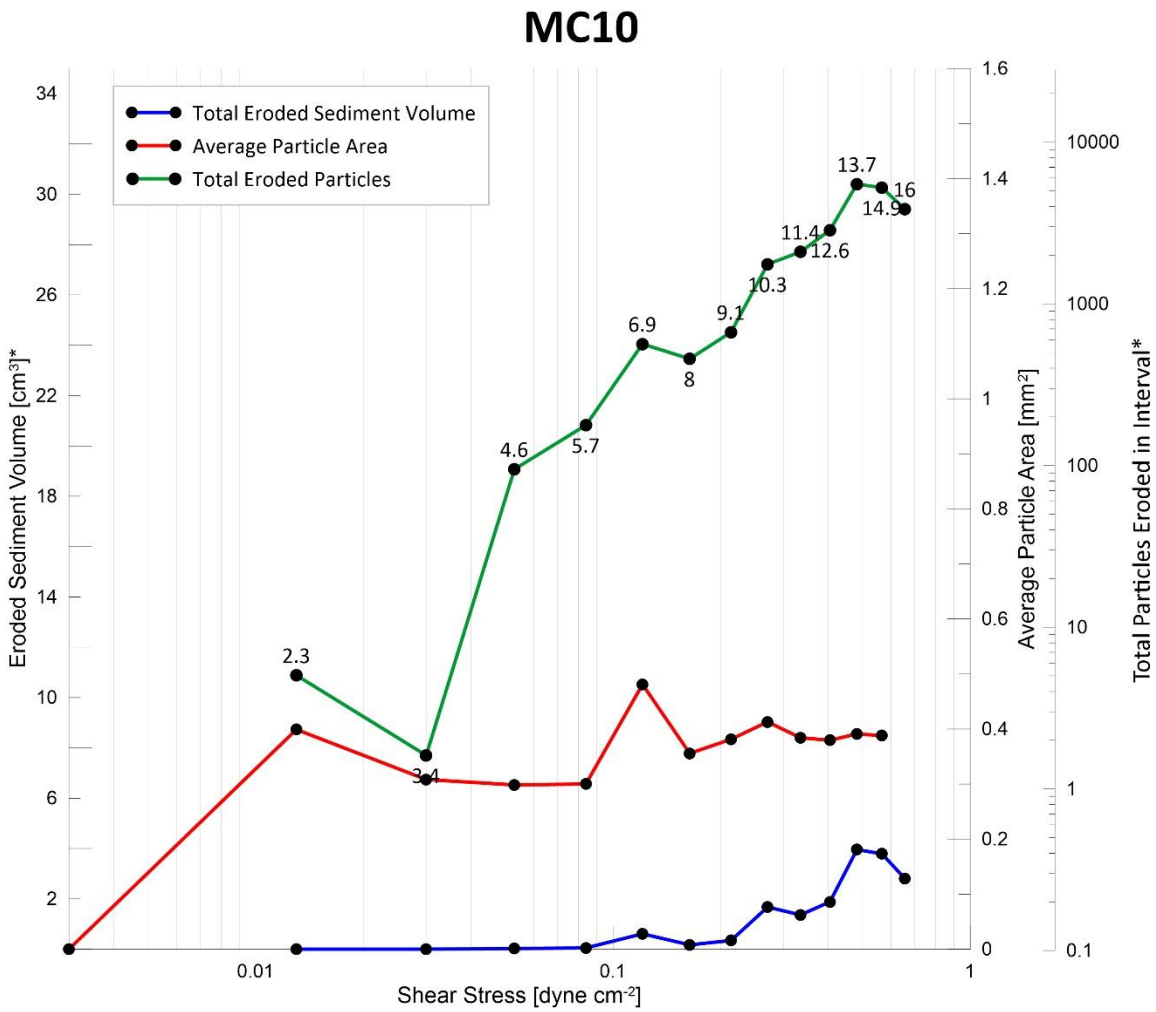

Figure B.8 *Erosion Graph of Core MC10*

Data points plotted in figure are sediment volume and particle counts per interval, normalized to 20 seconds, and average particle area per interval. These values were also calculated without the 0.0-0.2 mm size fraction as in earlier calculations. The red line is plotting average particle area (mm^2), the blue line shows normalized sediment volume (cm^3), and the green line shows normalized particle counts. Values listed on the particle counts line are flow speed values for each interval.

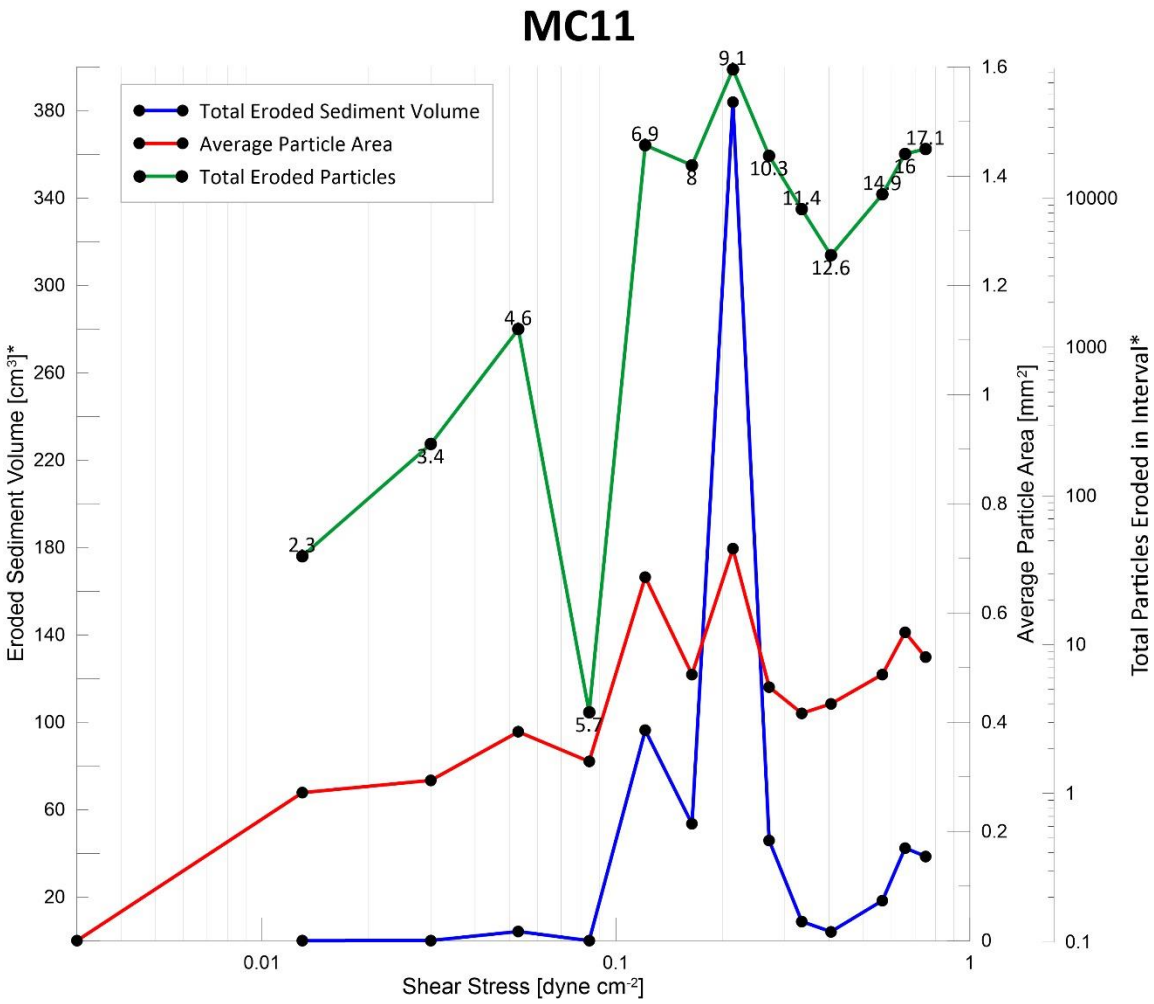

Figure B.9 *Erosion Graph of Core MC11*

Data points plotted in figure are sediment volume and particle counts per interval, normalized to 20 seconds, and average particle area per interval. These values were also calculated without the 0.0-0.2 mm size fraction as in earlier calculations. The red line is plotting average particle area (mm^2), the blue line shows normalized sediment volume (cm^3), and the green line shows normalized particle counts. Values listed on the particle counts line are flow speed values for each interval.

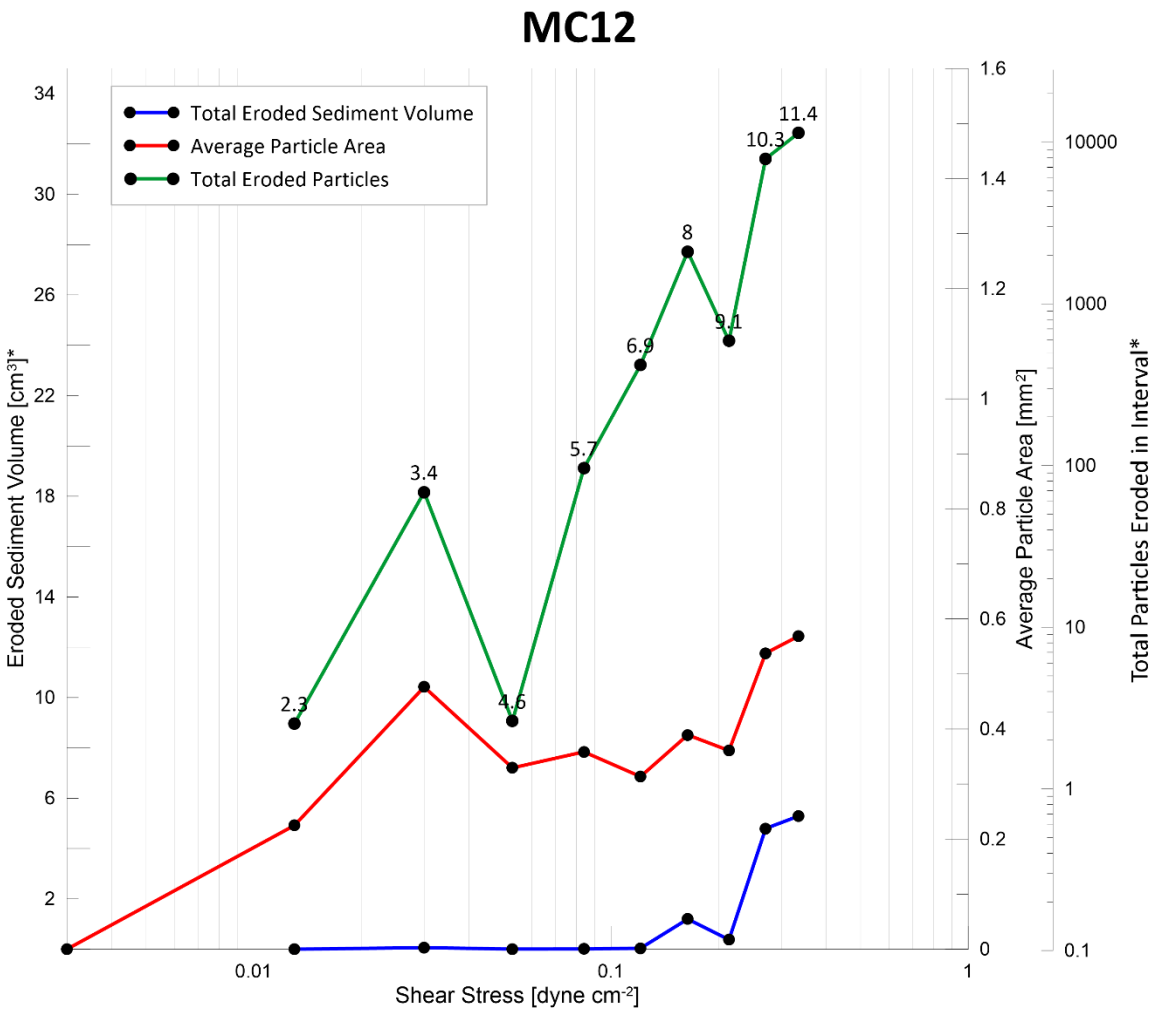

Figure B.10 *Erosion Graph of Core MC12*

Data points plotted in figure are sediment volume and particle counts per interval, normalized to 20 seconds, and average particle area per interval. These values were also calculated without the 0.0-0.2 mm size fraction as in earlier calculations. The red line is plotting average particle area (mm^2), the blue line shows normalized sediment volume (cm^3), and the green line shows normalized particle counts. Values listed on the particle counts line are flow speed values for each interval.

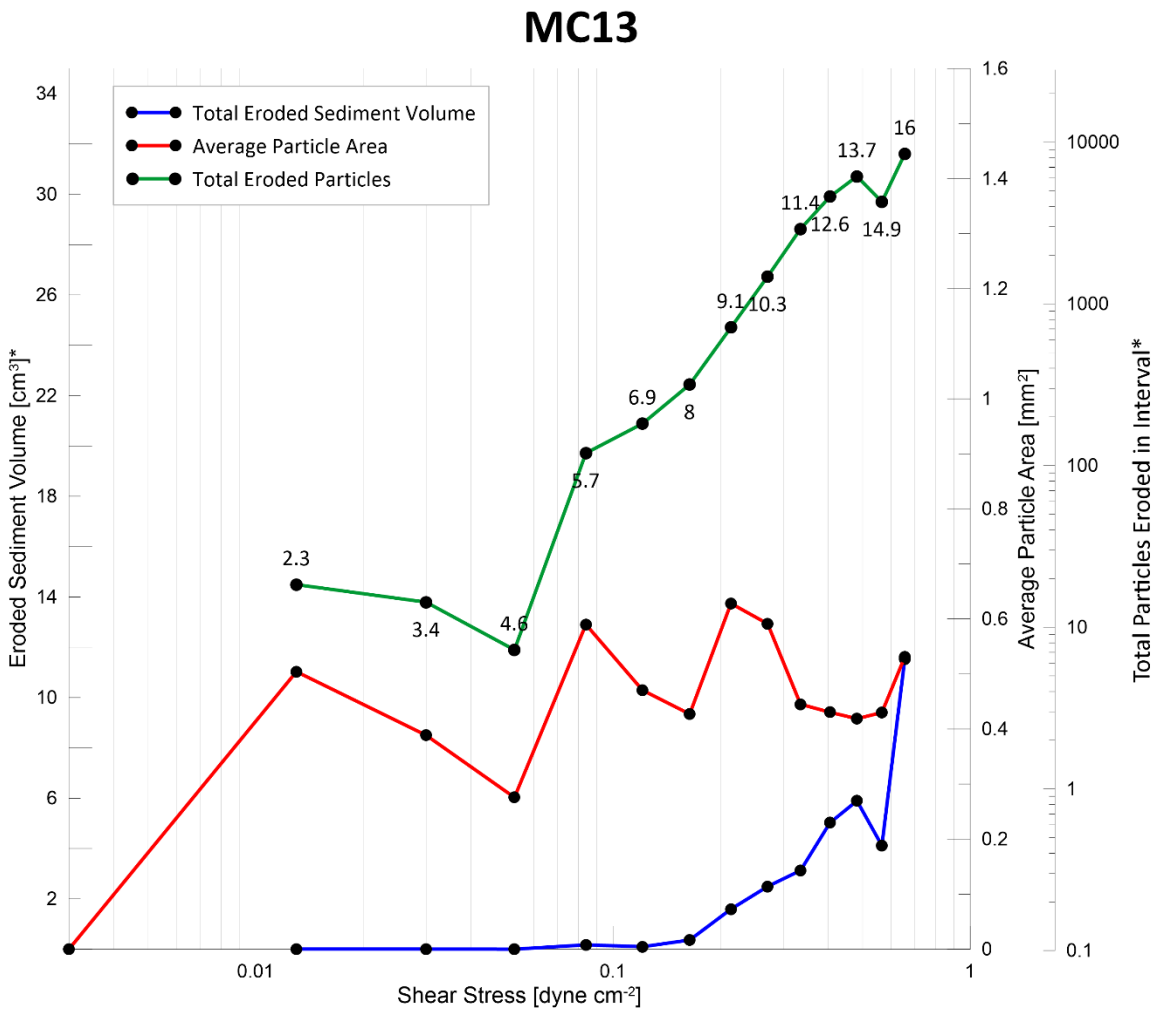

Figure B.11 *Erosion Graph of Core MC13*

Data points plotted in figure are sediment volume and particle counts per interval, normalized to 20 seconds, and average particle area per interval. These values were also calculated without the 0.0-0.2 mm size fraction as in earlier calculations. The red line is plotting average particle area (mm^2), the blue line shows normalized sediment volume (cm^3), and the green line shows normalized particle counts. Values listed on the particle counts line are flow speed values for each interval.

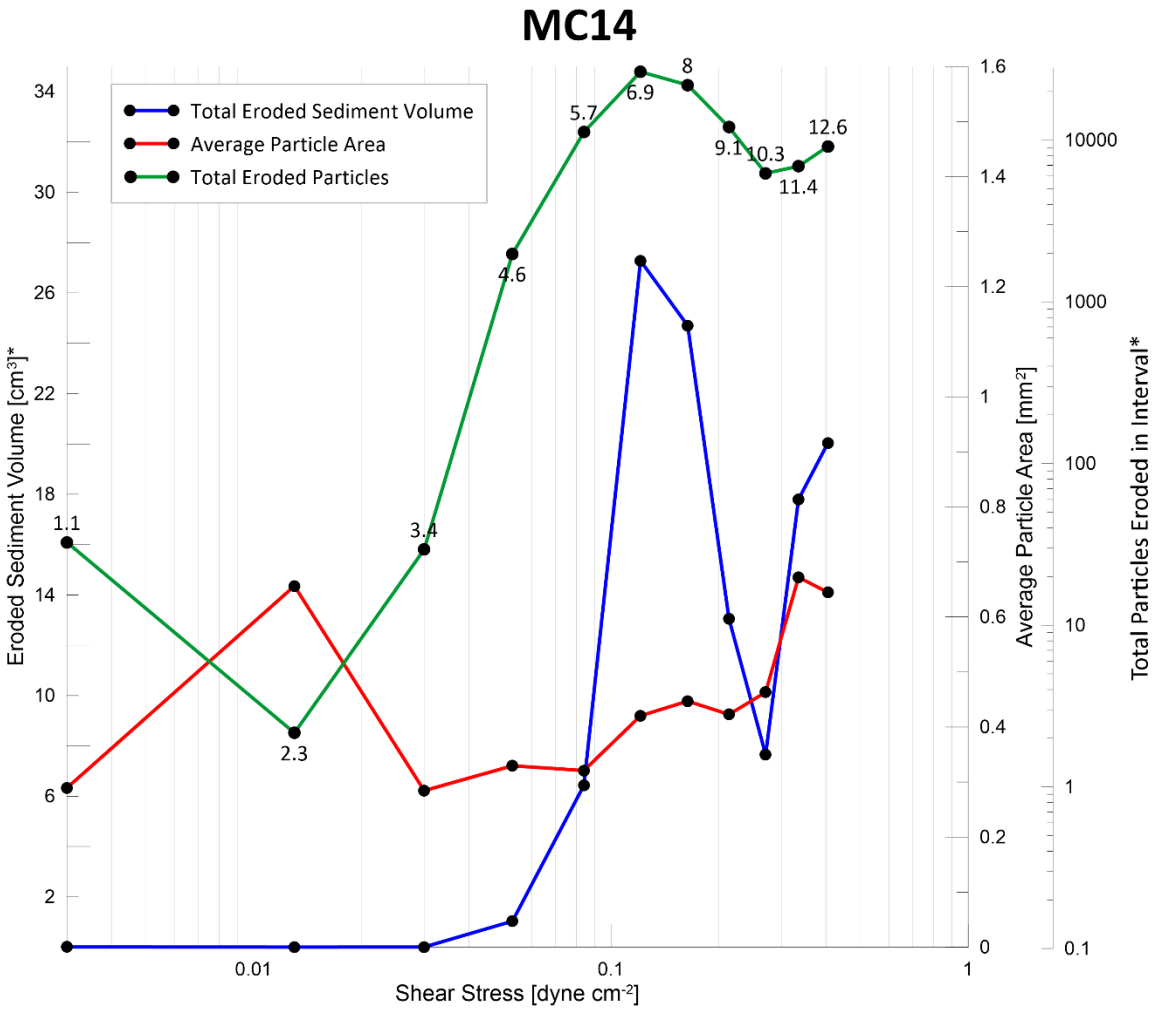

Figure B.12 *Erosion Graph of Core MC14*

Data points plotted in figure are sediment volume and particle counts per interval, normalized to 20 seconds, and average particle area per interval. These values were also calculated without the 0.0-0.2 mm size fraction as in earlier calculations. The red line is plotting average particle area (mm^2), the blue line shows normalized sediment volume (cm^3), and the green line shows normalized particle counts. Values listed on the particle counts line are flow speed values for each interval.

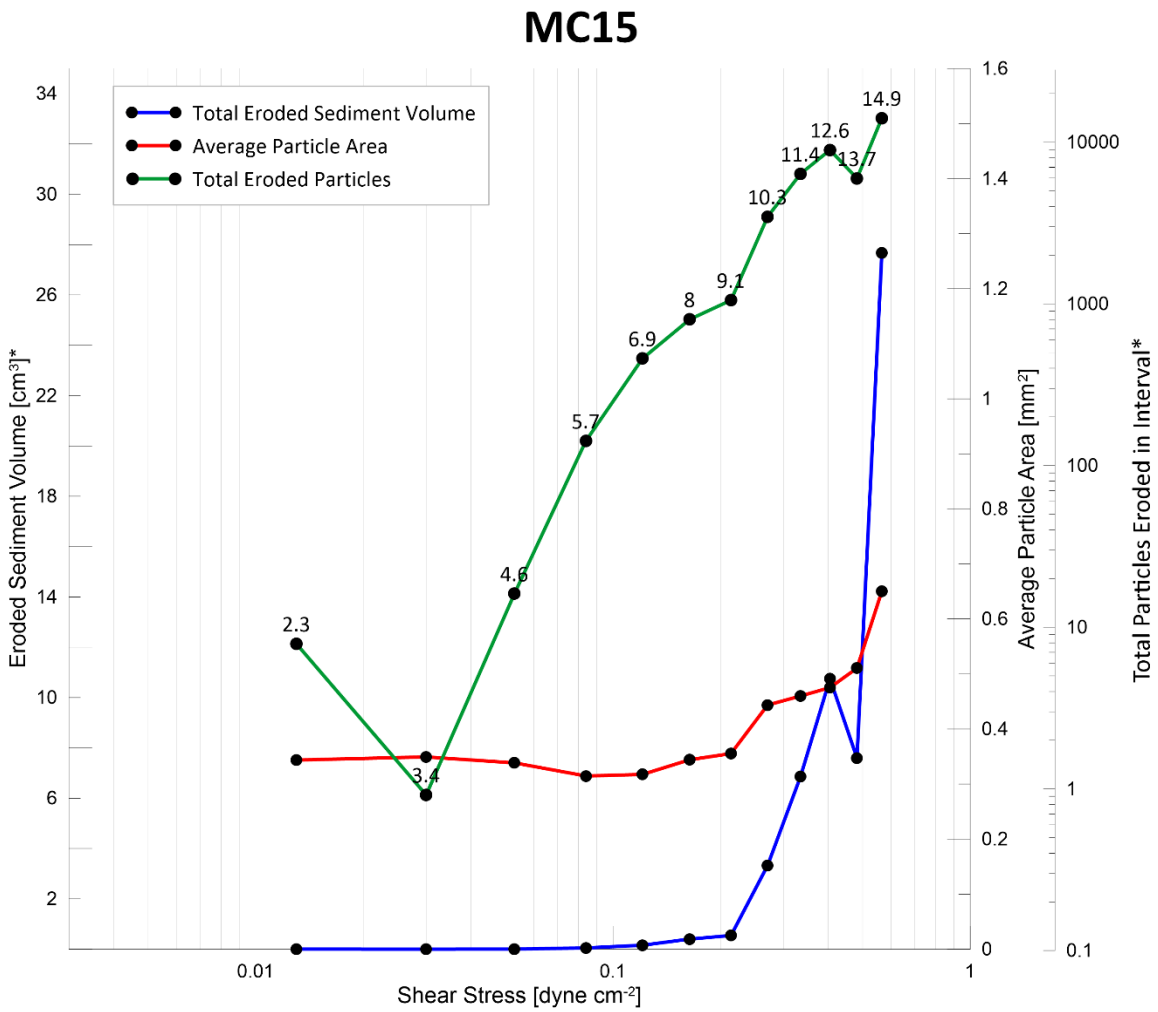

Figure B.13 *Erosion Graph of Core MC15*

Data points plotted in figure are sediment volume and particle counts per interval, normalized to 20 seconds, and average particle area per interval. These values were also calculated without the 0.0-0.2 mm size fraction as in earlier calculations. The red line is plotting average particle area (mm^2), the blue line shows normalized sediment volume (cm^3), and the green line shows normalized particle counts. Values listed on the particle counts line are flow speed values for each interval.

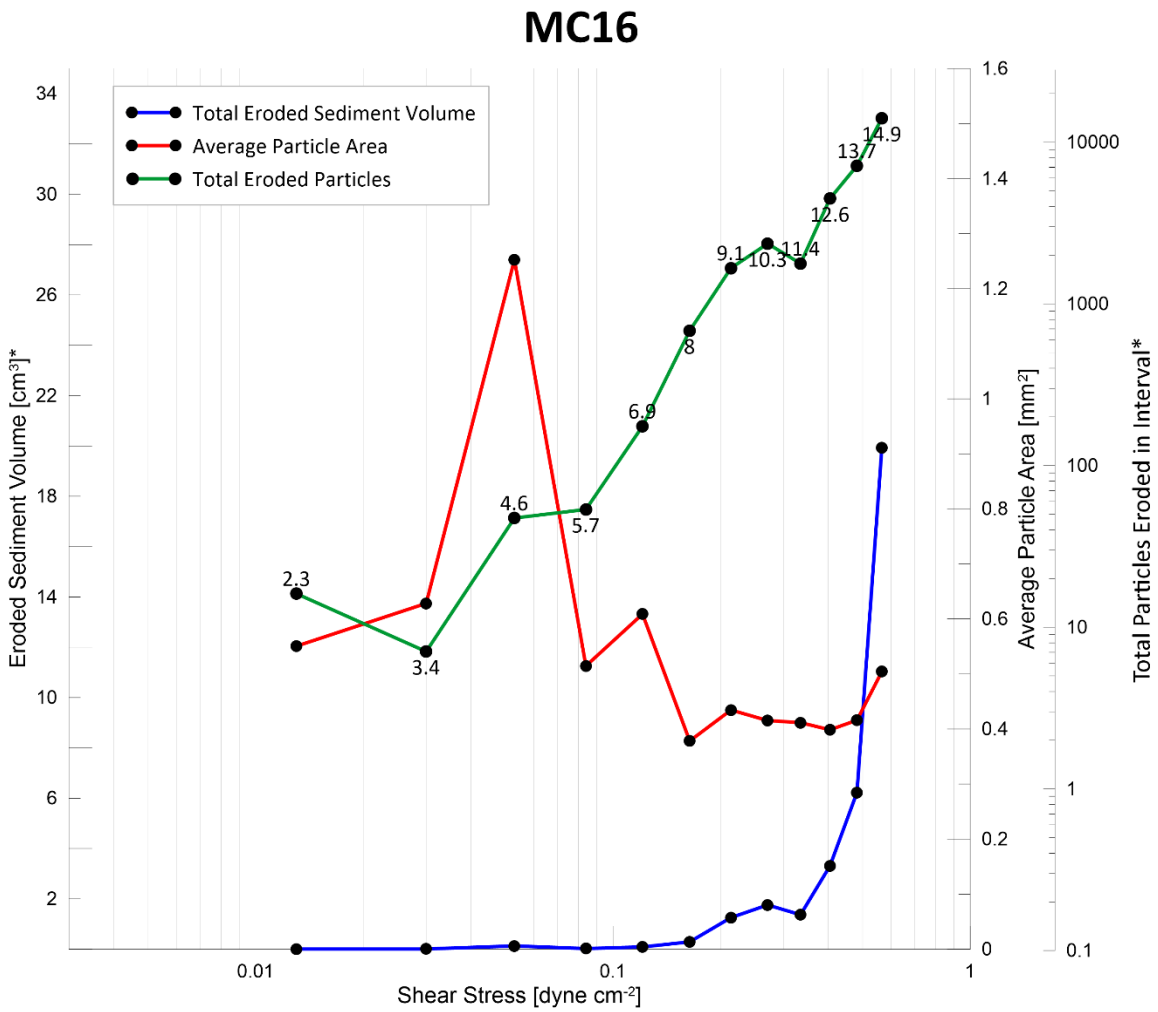

Figure B.14 *Erosion Graph of Core MC16*

Data points plotted in figure are sediment volume and particle counts per interval, normalized to 20 seconds, and average particle area per interval. These values were also calculated without the 0.0-0.2 mm size fraction as in earlier calculations. The red line is plotting average particle area (mm^2), the blue line shows normalized sediment volume (cm^3), and the green line shows normalized particle counts. Values listed on the particle counts line are flow speed values for each interval.

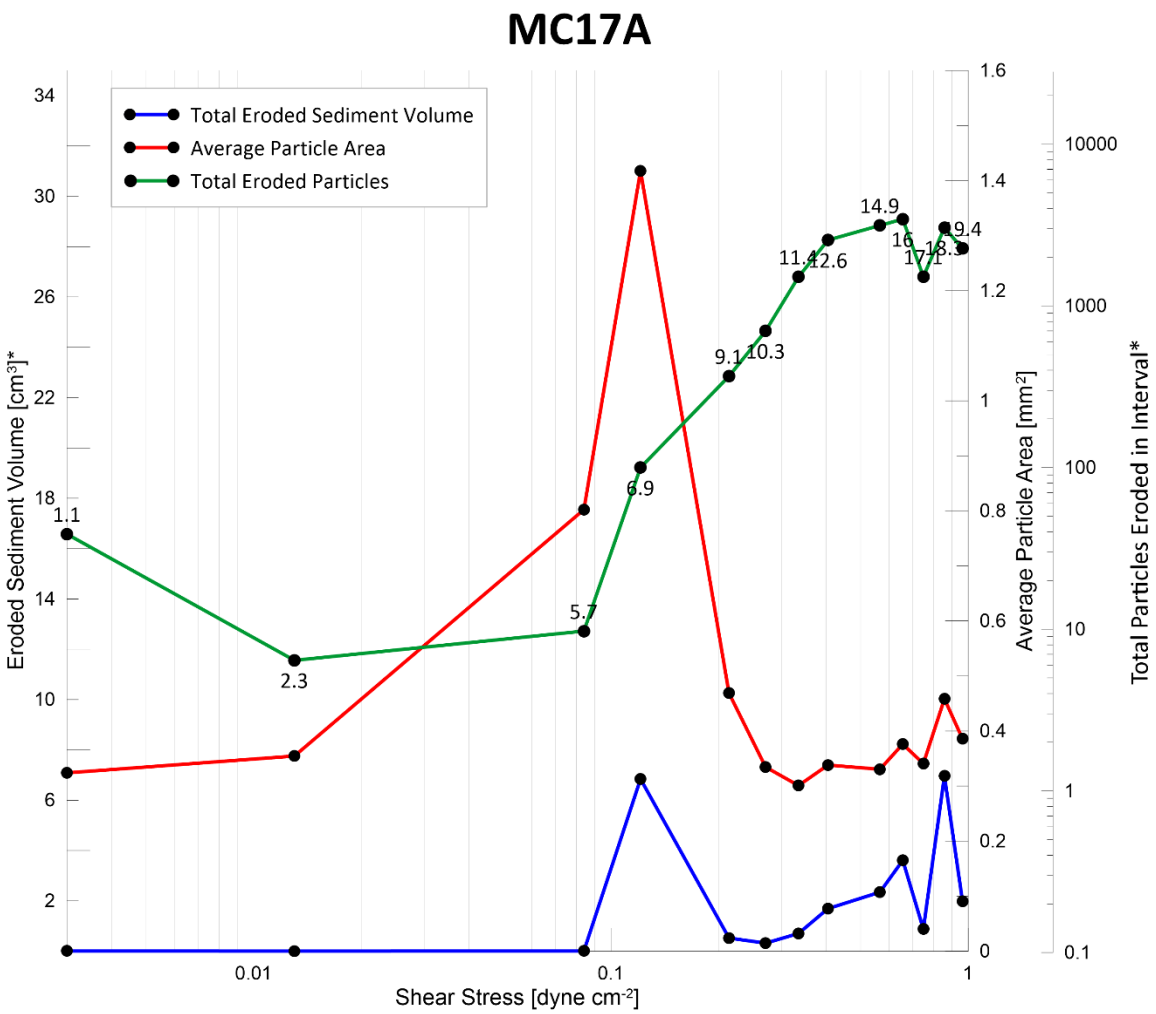

Figure B.15 *Erosion Graph of Core MC17A*

Data points plotted in figure are sediment volume and particle counts per interval, normalized to 20 seconds, and average particle area per interval. These values were also calculated without the 0.0-0.2 mm size fraction as in earlier calculations. The red line is plotting average particle area (mm^2), the blue line shows normalized sediment volume (cm^3), and the green line shows normalized particle counts. Values listed on the particle counts line are flow speed values for each interval.

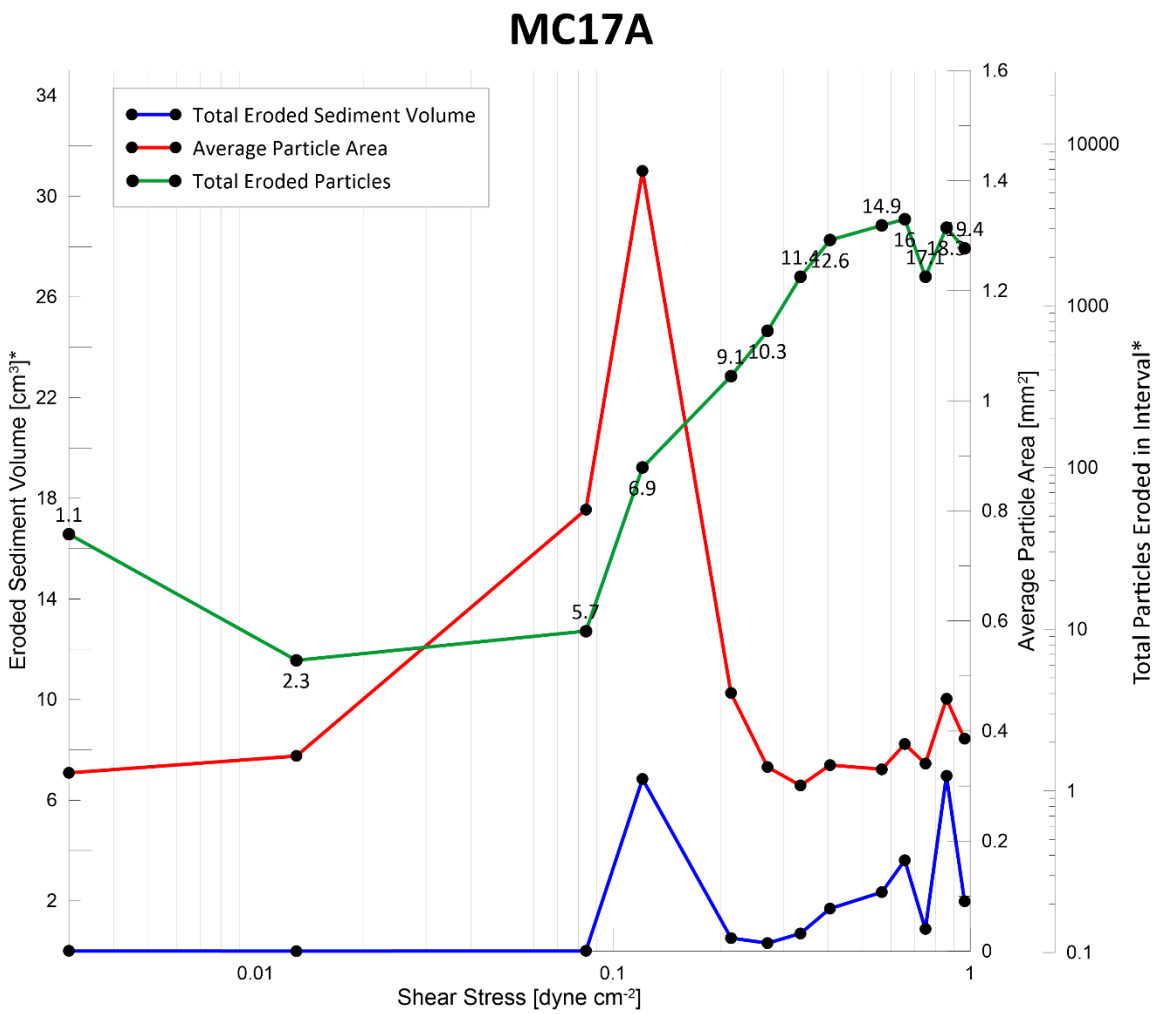

Figure B.16 *Erosion Graph of Core MC17B*

Data points plotted in figure are sediment volume and particle counts per interval, normalized to 20 seconds, and average particle area per interval. These values were also calculated without the 0.0-0.2 mm size fraction as in earlier calculations. The red line is plotting average particle area (mm^2), the blue line shows normalized sediment volume (cm^3), and the green line shows normalized particle counts. Values listed on the particle counts line are flow speed values for each interval.

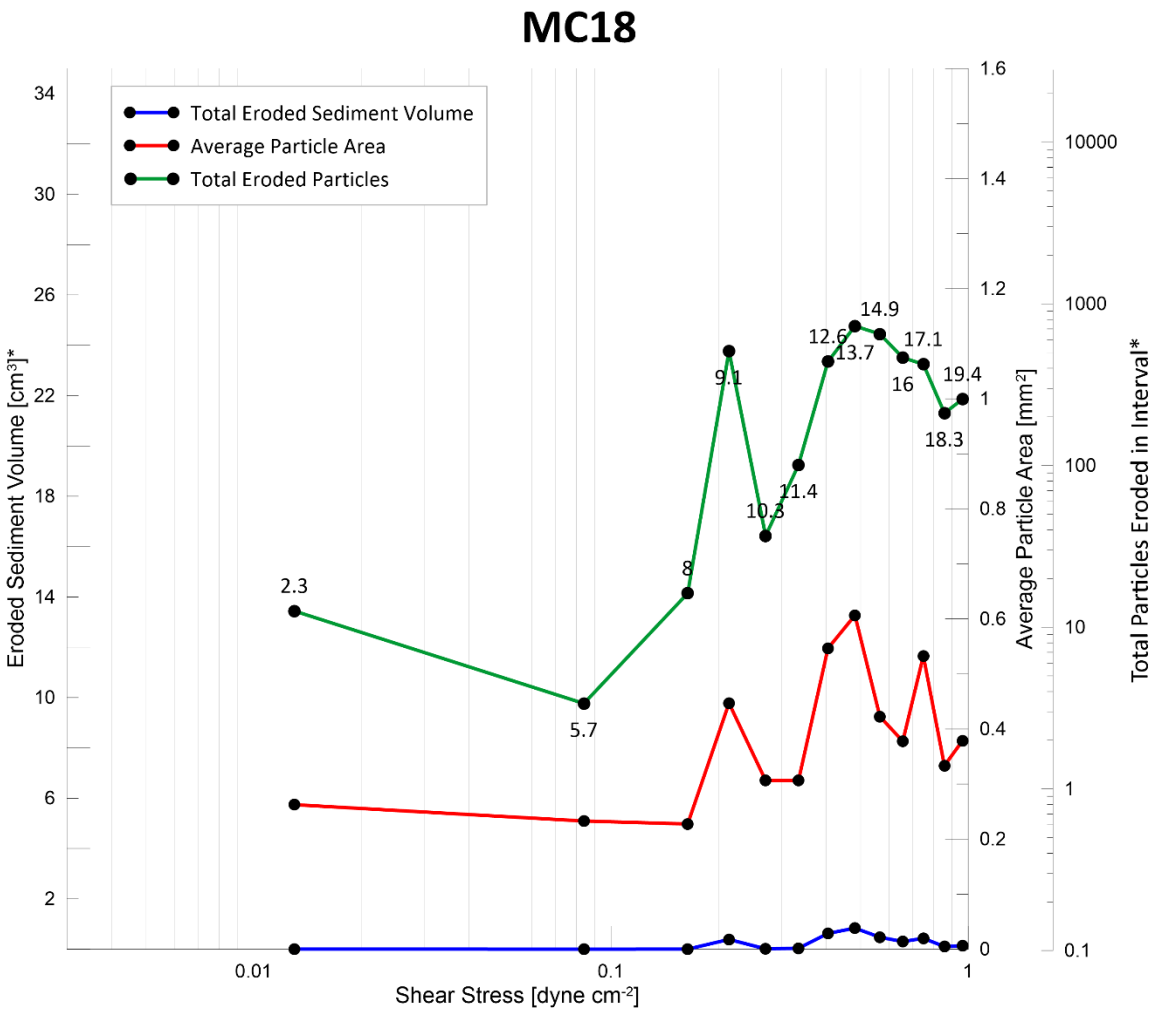

Figure B.17 *Erosion Graph of Core MC18*

Data points plotted in figure are sediment volume and particle counts per interval, normalized to 20 seconds, and average particle area per interval. These values were also calculated without the 0.0-0.2 mm size fraction as in earlier calculations. The red line is plotting average particle area (mm^2), the blue line shows normalized sediment volume (cm^3), and the green line shows normalized particle counts. Values listed on the particle counts line are flow speed values for each interval.

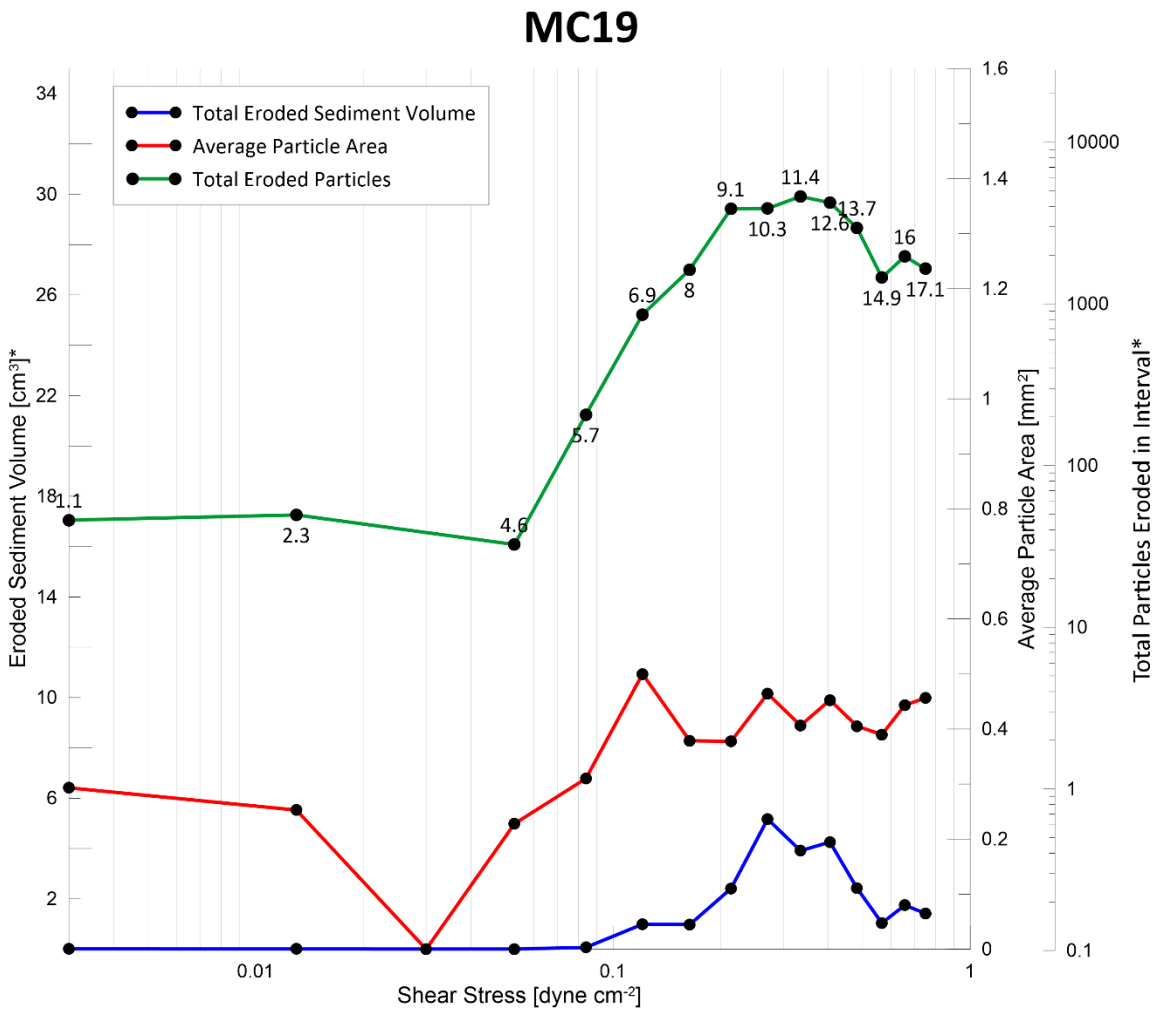

Figure B.18 *Erosion Graph of Core MC19*

Data points plotted in figure are sediment volume and particle counts per interval, normalized to 20 seconds, and average particle area per interval. These values were also calculated without the 0.0-0.2 mm size fraction as in earlier calculations. The red line is plotting average particle area (mm^2), the blue line shows normalized sediment volume (cm^3), and the green line shows normalized particle counts. Values listed on the particle counts line are flow speed values for each interval.

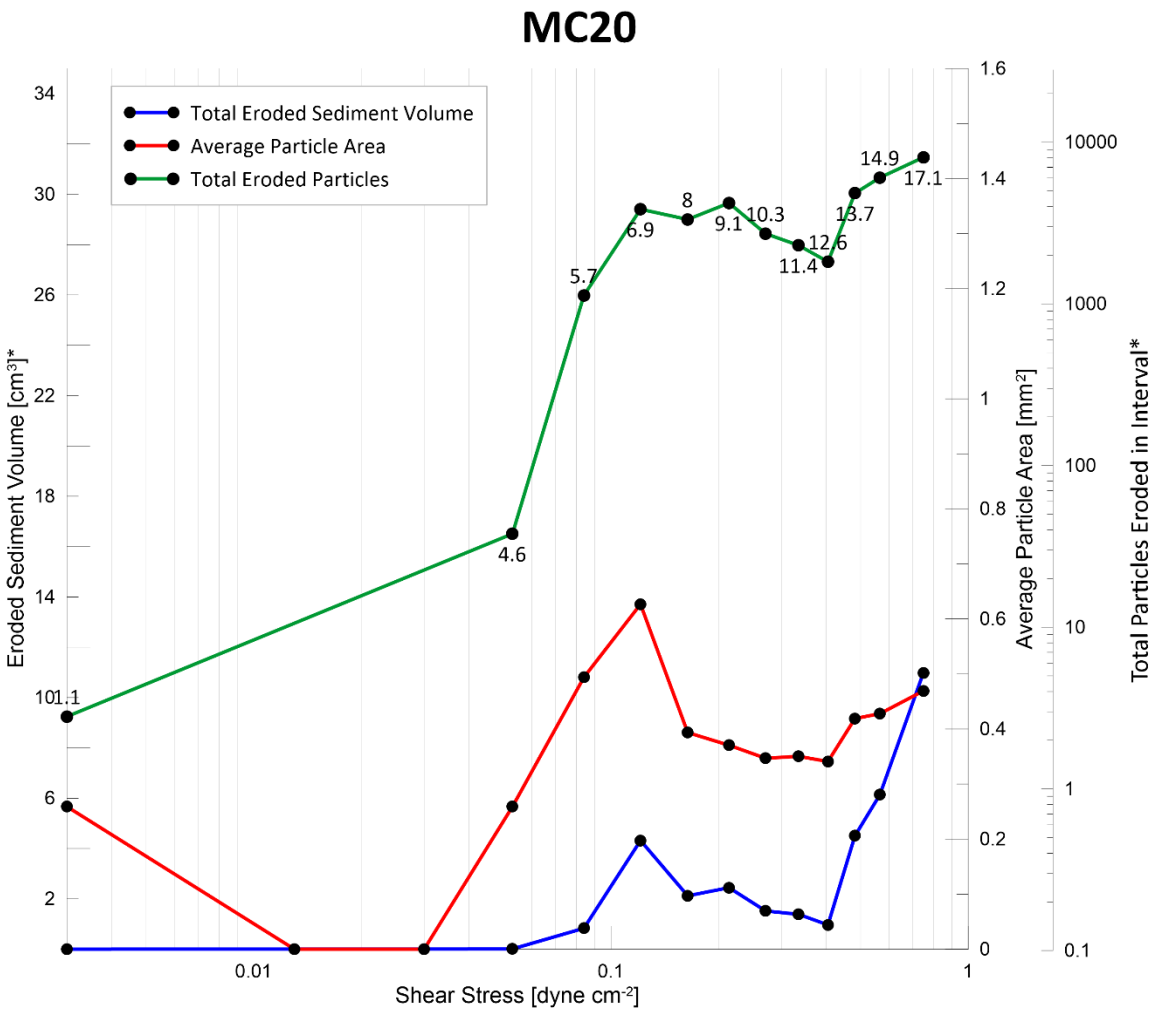

Figure B.19 *Erosion Graph of Core MC20*

Data points plotted in figure are sediment volume and particle counts per interval, normalized to 20 seconds, and average particle area per interval. These values were also calculated without the 0.0-0.2 mm size fraction as in earlier calculations. The red line is plotting average particle area (mm^2), the blue line shows normalized sediment volume (cm^3), and the green line shows normalized particle counts. Values listed on the particle counts line are flow speed values for each interval.

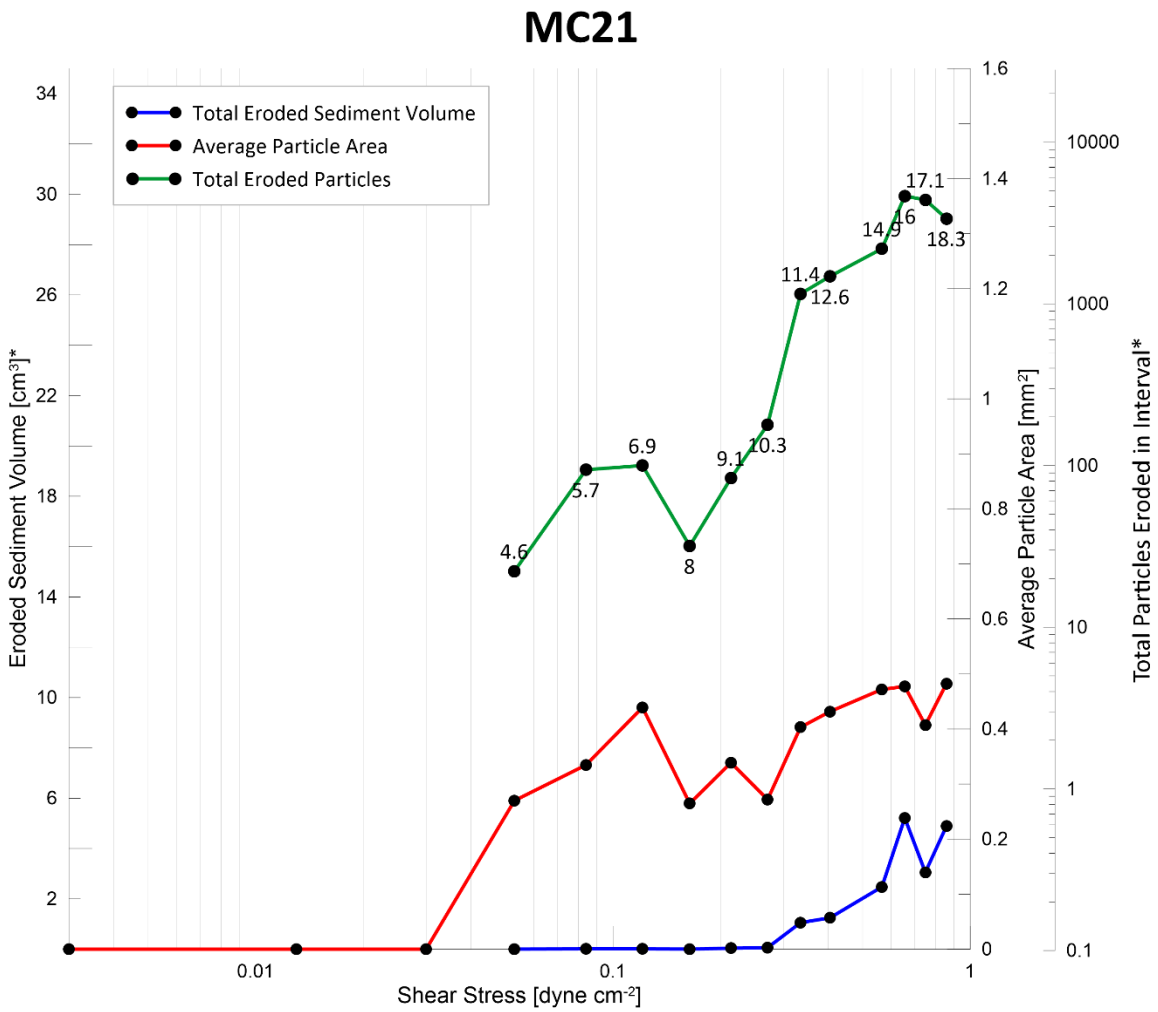

Figure B.20 *Erosion Graph of Core MC21*

Data points plotted in figure are sediment volume and particle counts per interval, normalized to 20 seconds, and average particle area per interval. These values were also calculated without the 0.0-0.2 mm size fraction as in earlier calculations. The red line is plotting average particle area (mm^2), the blue line shows normalized sediment volume (cm^3), and the green line shows normalized particle counts. Values listed on the particle counts line are flow speed values for each interval.

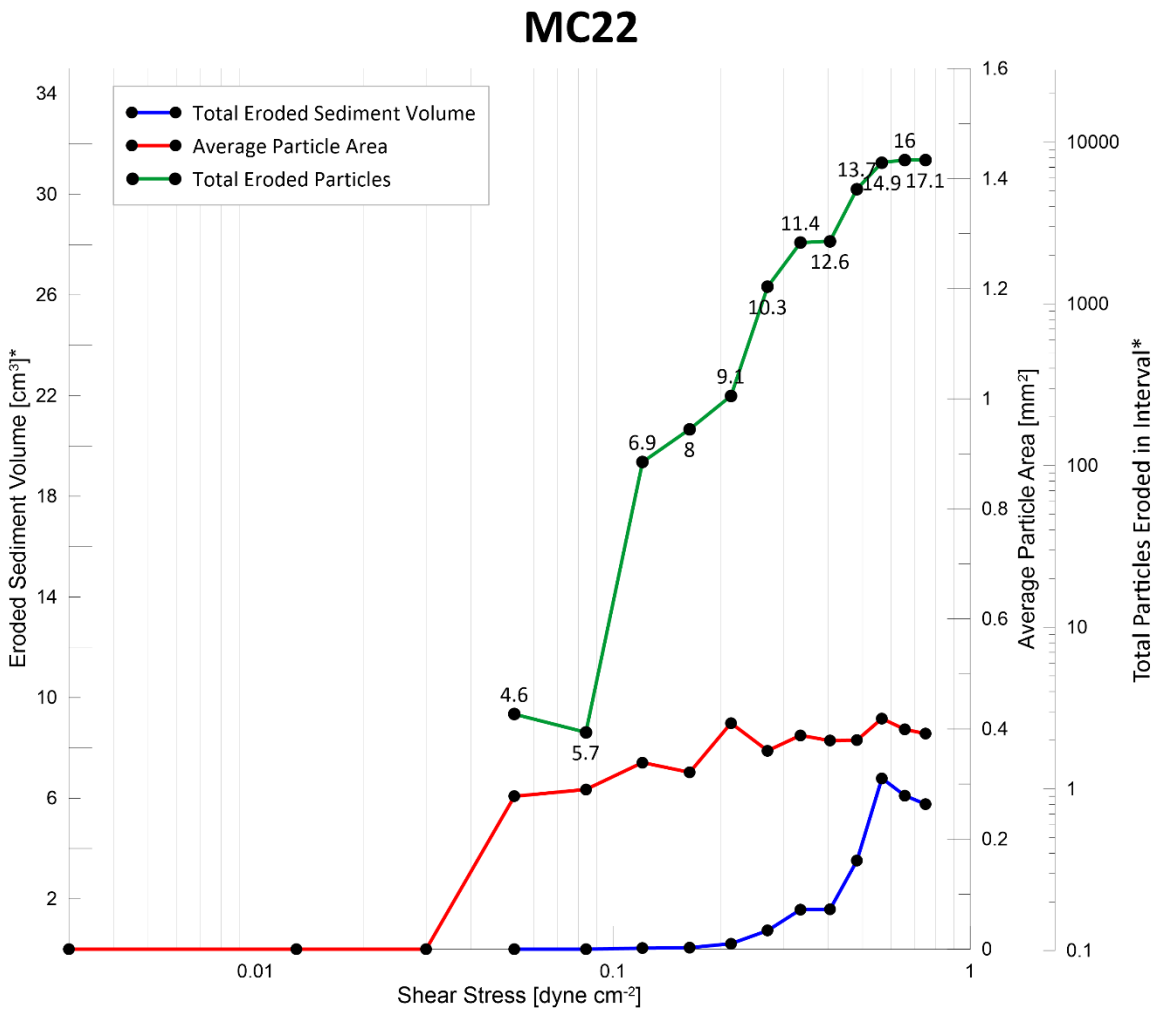

Figure B.21 *Erosion Graph of Core MC22*

Data points plotted in figure are sediment volume and particle counts per interval, normalized to 20 seconds, and average particle area per interval. These values were also calculated without the 0.0-0.2 mm size fraction as in earlier calculations. The red line is plotting average particle area (mm^2), the blue line shows normalized sediment volume (cm^3), and the green line shows normalized particle counts. Values listed on the particle counts line are flow speed values for each interval.

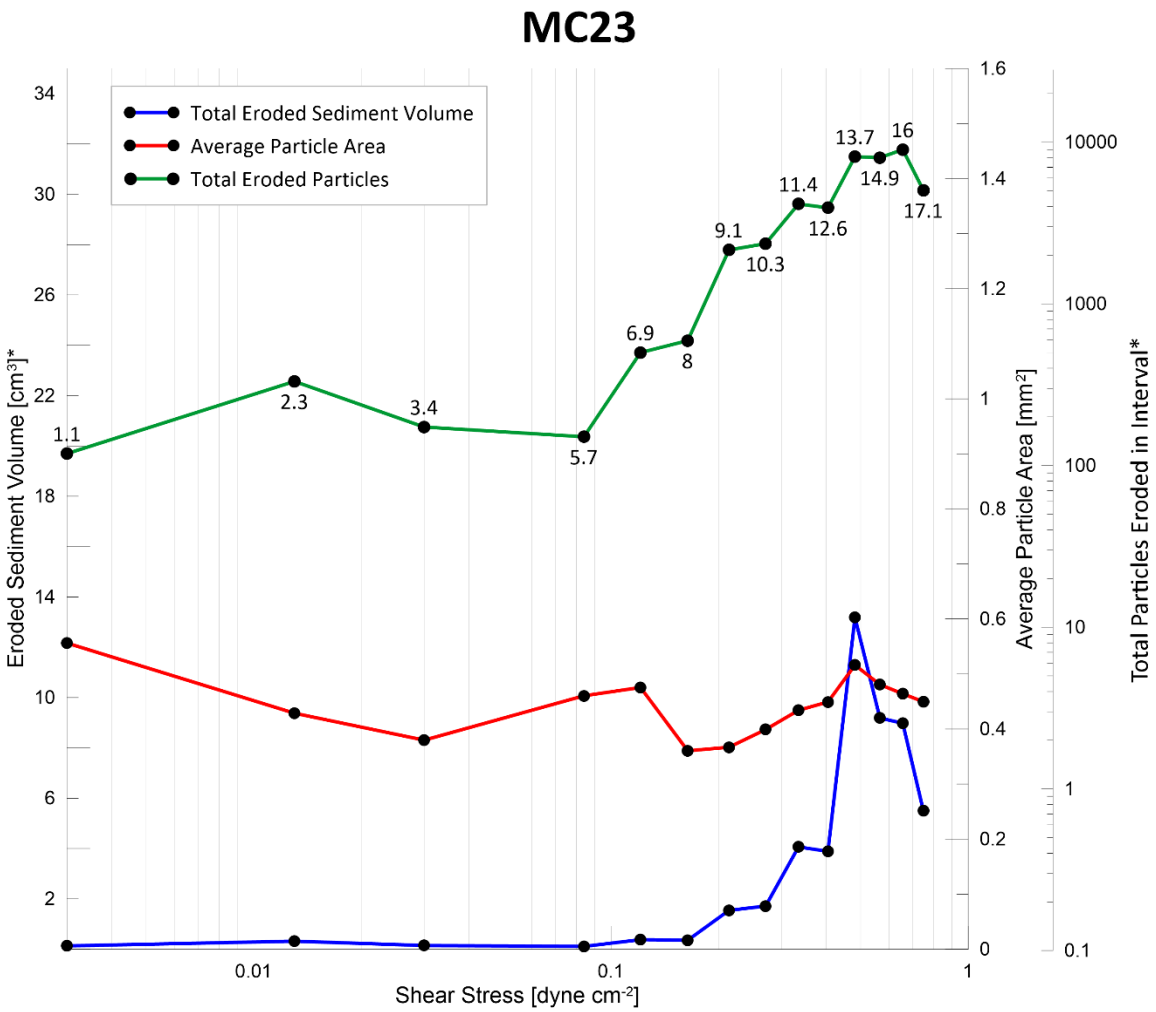

Figure B.22 *Erosion Graph of Core MC23*

Data points plotted in figure are sediment volume and particle counts per interval, normalized to 20 seconds, and average particle area per interval. These values were also calculated without the 0.0-0.2 mm size fraction as in earlier calculations. The red line is plotting average particle area (mm^2), the blue line shows normalized sediment volume (cm^3), and the green line shows normalized particle counts. Values listed on the particle counts line are flow speed values for each interval.

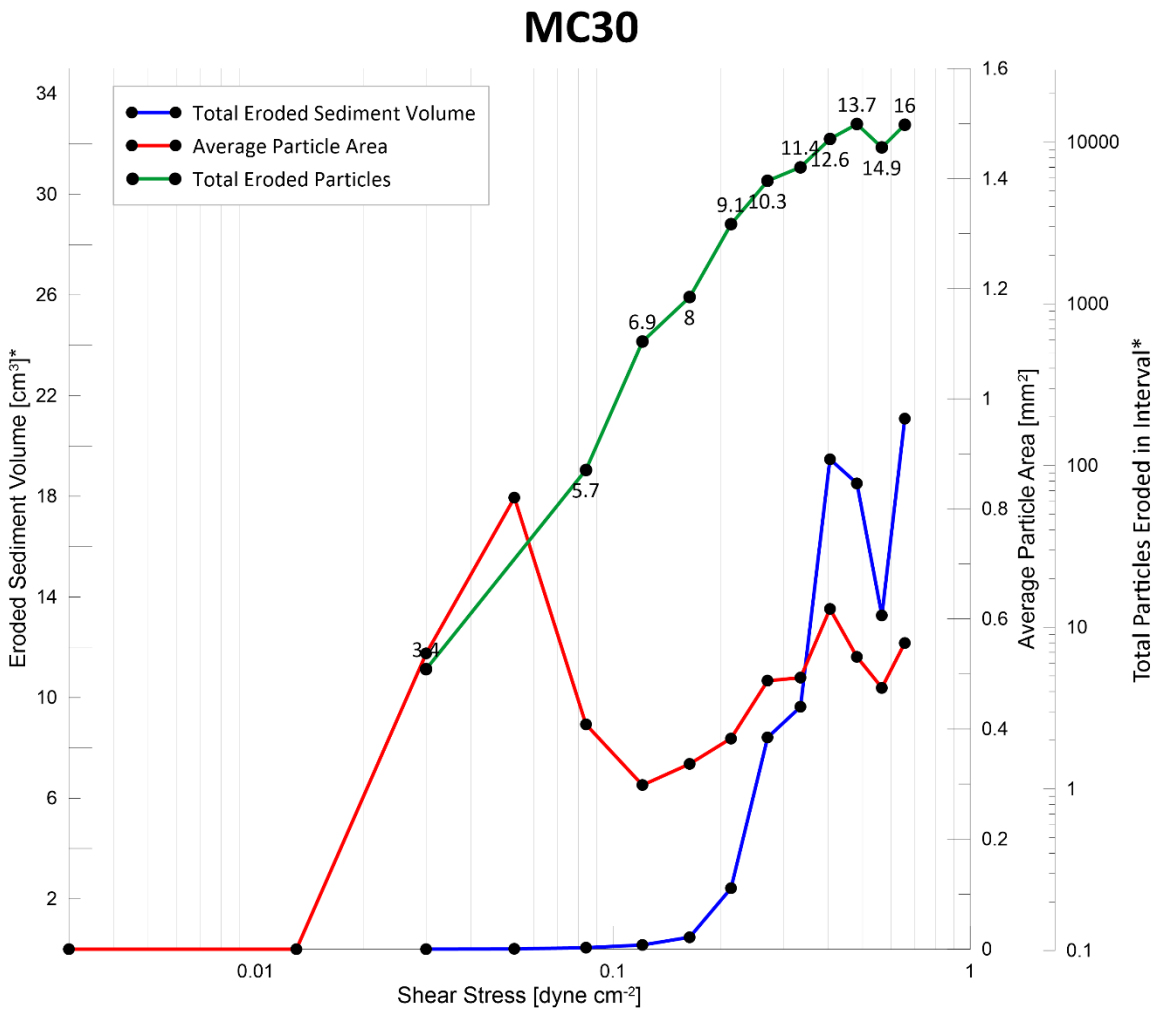

Figure B.23 *Erosion Graph of Core MC30*

Data points plotted in figure are sediment volume and particle counts per interval, normalized to 20 seconds, and average particle area per interval. These values were also calculated without the 0.0-0.2 mm size fraction as in earlier calculations. The red line is plotting average particle area (mm^2), the blue line shows normalized sediment volume (cm^3), and the green line shows normalized particle counts. Values listed on the particle counts line are flow speed values for each interval.

REFERENCES

Amos, C. L.; Bergamasco, A.; Umgiesser, G.; Cappucci, S.; Cloutier, D.; DeNat, L.; Flindt, M.; Bonardi, M.; Cristante, S. The Stability of Tidal Flats in Venice Lagoon—the Results of in-Situ Measurements Using Two Benthic, Annular Flumes. *Journal of Marine Systems* **2004**, *51* (1), 211–241. https://doi.org/10.1016/j.jmarsys.2004.05.013.

Appleby, P. G.; Oldfieldz, F. The Assessment of 210Pb Data from Sites with Varying Sediment Accumulation Rates. *Hydrobiologia* **1983**, *103* (1), 29–35. https://doi.org/10.1007/BF00028424.

Baskaran, M.; Nix, J.; Kuyper, C.; Karunakara, N. Problems with the Dating of Sediment Core Using Excess 210Pb in a Freshwater System Impacted by Large Scale Watershed Changes. *Journal of Environmental Radioactivity* **2014**, *138*, 355–363. https://doi.org/10.1016/j.jenvrad.2014.07.006.

Binford, M. W. Calculation and Uncertainty Analysis of 210Pb Dates for PRILA Project Lake Sediment Cores. *J Palealimnol 3*, 253-267. Doi: 10.1007/BF00219461.

Borrowman, T. D.; Smith, E. R.; Gailani, J. Z.; Caviness, L. *Erodibility Study of Passaic River Sediments Using USACE Sedflume:*; Defense Technical Information Center: Fort Belvoir, VA, 2006. https://doi.org/10.21236/ADA456816.

Brooks, G. R.; Larson, R. A.; Schwing, P. T.; Romero, I.; Moore, C.; Reichart, G.-J.; Jilbert, T.; Chanton, J. P.; Hastings, D. W.; Overholt, W. A.; Marks, K. P.; Kostka, J. E.; Holmes, C. W.; Hollander, D. Sedimentation Pulse in the NE Gulf of Mexico Following the 2010 DWH Blowout. *PLOS ONE* **2015**, *10* (7), e0132341. https://doi.org/10.1371/journal.pone.0132341.

Chanton, J. P.; Cherrier, J.; Wilson, R. M.; Sarkodee-Adoo, J.; Bosman, S.; Mickle, A.; Graham, W. M. Radiocarbon Evidence That Carbon from the Deepwater Horizon Spill Entered the Planktonic Food Web of the Gulf of Mexico. *Environ. Res. Lett.* **2012**, *7* (4), 045303. https://doi.org/10.1088/1748-9326/7/4/045303.

Chanton, J. P.; Giering, S. L. C.; Bosman, S. H.; Rogers, K. L.; Sweet, J.; Asper, V. L.; Diercks, A. R.; Passow, U. Isotopic Composition of Sinking Particles: Oil Effects, Recovery and Baselines in the Gulf of Mexico, 2010–2015. *Elementa: Science of the Anthropocene* **2018**, *6* (43). https://doi.org/10.1525/elementa.298.

Chanton, J.; Zhao, T.; Rosenheim, B. E.; Joye, S.; Bosman, S.; Brunner, C.; Yeager, K. M.; Diercks, A. R.; Hollander, D. Using Natural Abundance Radiocarbon To Trace the Flux of Petrocarbon to the Seafloor Following the Deepwater Horizon Oil Spill. *Environ. Sci. Technol.* **2015**, *49* (2), 847–854. https://doi.org/10.1021/es5046524.

Coleman, J. M., Bouma, A. H., Roberts, H. H., and Thayer, P. A. (1986). Stratification in 764 Mississippi Fan Cores Revealed by X-Ray Radiography. In 765 doi:10.2973/dsdp.proc.96.123.1986.

Daly, K. L.; Passow, U.; Chanton, J.; Hollander, D. Assessing the Impacts of Oil-Associated Marine Snow Formation and Sedimentation during and after the Deepwater Horizon Oil Spill. *Anthropocene* **2016**, *13*, 18–33. https://doi.org/10.1016/j.ancene.2016.01.006.

Diercks, A.-R.; Dike, C.; Asper, V. L.; DiMarco, S. F.; Chanton, J. P.; Passow, U. Scales of Seafloor Sediment Resuspension in the Northern Gulf of Mexico. *Elem Sci Anth* **2018**, *6* (1), 32. https://doi.org/10.1525/elementa.285.

Diercks, A.-R.; Highsmith, R. C.; Asper, V. L.; Joung, D.; Zhou, Z.; Guo, L.; Shiller, A. M.; Joye, S. B.; Teske, A. P.; Guinasso, N.; Wade, T. L.; Lohrenz, S. E. Characterization of Subsurface Polycyclic Aromatic Hydrocarbons at the Deepwater Horizon Site. *Geophysical Research Letters* **2010**, *37* (20). https://doi.org/10.1029/2010GL045046.

Diercks, A.-R.; Romero, **I.R.;** Larson, **R.A.;** Schwing**, P.;** Harris**, A.;** Bosman, **S.;** Chanton, **J.P.;** Brooks**,** G.; Resuspension, Redistribution and Deposition of oil-residues to offshore Depocenters after the Deepwater Horizon oil spill. *Frontiers in Marine Science*. ***In Revision***

Fan, W.; McGuire, J.; Shearer, P. Abundant Spontaneous and Dynamically Triggered Submarine Landslides in the Gulf of Mexico. *Geophysical Research Letters* **2020**, *47*. https://doi.org/10.1029/2020GL087213.

Gardner, W. D.; Sullivan, L. G. Benthic Storms: Temporal Variability in a Deep-Ocean Nepheloid Layer. *Science* **1981**, *213* (4505), 329–331.

Gardner, W.; Biscaye, P.; Richardson, M. Sediment Trapping in High Energy Environments. *EOS* **1983**, *63*.

Gardner, W. D.; Tucholke, B. E.; Richardson, M. J.; Biscaye, P. E. Benthic Storms, Nepheloid Layers, and Linkage with Upper Ocean Dynamics in the Western North Atlantic. *Marine Geology* **2017**, *385*, 304–327. https://doi.org/10.1016/j.margeo.2016.12.012.

Giering, S. L. C.; Yan, B.; Asper, V.; Diercks, A.-R.; Chanton, J.; Pitiranggon, M.; Passow, U. The Ecosystem Baseline for Particle Flux in the Northern Gulf of Mexico. *Elementa: Science of the Anthropocene* **2018**, *6* (6).

Gust, G.; Morris, M. J. Erosion Thresholds and Entrainment Rates of Undisturbed in Situ Sediments. *Journal of Coastal Research* **1989**, 87–99.

Harris, P. T. Shelf and Deep-Sea Sedimentary Environments and Physical Benthic Disturbance Regimes: A Review and Synthesis. *Marine Geology* **2014**, *353*, 169–184. https://doi.org/10.1016/j.margeo.2014.03.023.

Hayter, E.; Gustavson, K.; Ells, S.; Gailani, J.; Wolfe, J.; Dekker, T.; Redder, T. *Technical Guidelines on Performing a Sediment Erosion and Deposition Assessment (SEDA) at Superfund Sites:*; Defense Technical Information Center: Fort Belvoir, VA, 2014. https://doi.org/10.21236/ADA610123.

Isley, A. E.; Dale Pillsbury, R.; Laine, E. P. The Genesis and Character of Benthic Turbid Events, Northern Hatteras Abyssal Plain. *Deep Sea Research Part A. Oceanographic Research Papers* **1990**, *37* (7), 1099–1119. https://doi.org/10.1016/0198-0149(90)90053-X.

Jochens, A. E.; DiMarco, S. F. Physical Oceanographic Conditions in the Deepwater Gulf of Mexico in Summer 2000–2002. *Deep Sea Research Part II: Topical Studies in Oceanography* **2008**, *55* (24), 2541–2554. https://doi.org/10.1016/j.dsr2.2008.07.003.

Jonsson, P. R.; van Duren, L. A.; Amielh, M.; Asmus, R.; Aspden, R. J.; Daunys, D.; Friedrichs, M.; Friend, P. L.; Olivier, F.; Pope, N.; Precht, E.; Sauriau, P.-G.; Schaaff, E. Making Water Flow: A Comparison of the Hydrodynamic Characteristics of 12 Different Benthic Biological Flumes. *Aquat Ecol* **2006**, *40* (4), 409–438. https://doi.org/10.1007/s10452-006-9049-z.

Kitto, M. Determination of Photon Self-Absorption Corrections for Soil Samples. *International Journal of Radiation Applications and Instrumentation. Part A. Applied Radiation and Isotopes* **1991**, *42*, 835–839. https://doi.org/10.1016/0883-2889(91)90221-L.

Kramer, K. V.; Shedd, W. W. A 1.4-Billion-Pixel Map of the Gulf of Mexico Seafloor. 2017. https://eos.org/science-updates/a-1-4-billion-pixel-map-of-the-gulf-of-mexico-seafloor (accessed Aug 12, 2020).

Laine, E. P.; Gardner, W. D.; Jo Richardson, M.; Kominz, M. Abyssal Currents and Advection of Resuspended Sediment along the Northeastern Bermuda Rise. *Marine Geology* **1994**, *119* (1–2), 159–171. https://doi.org/10.1016/0025-3227(94)90146-5.

Lampitt, R. S. Evidence for the Seasonal Deposition of Detritus to the Deep-Sea Floor and Its Subsequent Resuspension. *Deep Sea Research Part A. Oceanographic Research Papers* **1985**, *32* (8), 885–897. https://doi.org/10.1016/0198-0149(85)90034-2.

Larson, R. A.; Brooks, G. R.; Schwing, P. T.; Holmes, C. W.; Carter, S. R.; Hollander, D. J. High-Resolution Investigation of Event Driven Sedimentation: Northeastern Gulf of Mexico. *Anthropocene* **2018**, *24*, 40–50. https://doi.org/10.1016/j.ancene.2018.11.002.

Lehr, B.; Bristol, S.; Possolo, A. *Oil Budget Calculator Deepwater Horizon*; Technical Documentation; The Federal Interagency Solutions Group, Oil Budget Calculator Science and Engineering Team, 2010; p 217.

MacDonald, I. R.; Garcia-Pineda, O.; Beet, A.; Daneshgar Asl, A.; Feng, L.; Graettinger, G.; French-McCay, D.; Holmes, J.; Hu, C.; Huffer, F.; Leifer, I.; Muller-Karger, F.; Solow, A.; Silva, M.; Swayze, G. Natural and Unnatural Oil Slicks in the Gulf

of Mexico - MacDonald - 2015 - Journal of Geophysical Research: Oceans - Wiley Online Library https://agupubs.onlinelibrary.wiley.com/doi/full/10.1002/2015JC011062 (accessed Jun 15, 2020).

McCave, I. N.; Hall, I. R. Size sorting in marine muds: Processes, pitfalls, and prospects for paleoflow-speed proxies - McCave - 2006 - Geochemistry, Geophysics, Geosystems - Wiley Online Library https://agupubs.onlinelibrary.wiley.com/doi/full/10.1029/2006gc001284 (accessed Aug 12, 2020).

McCave, I. N.; Hollister, C. D. Sedimentation under Deep-Sea Current Systems: Pre-HEBBLE Ideas. *Marine Geology* **1985**, *66* (1), 13–24. https://doi.org/10.1016/0025-3227(85)90020-9.

McNeil, J.; Taylor, C.; Lick, W. Measurements of Erosion of Undisturbed Bottom Sediments with Depth. *Journal of Hydraulic Engineering* **1996**, *122* (6), 316–324. https://doi.org/10.1061/(ASCE)0733-9429(1996)122:6(316).

Morey, S.; Gopalakrishnan, G.; Pallàs-Sanz, E.; Azevedo Correia de Souza, J. M.; Donohue, K.; Pérez-Brunius, P.; Dukhovskoy, D.; Chassignet, E.; Cornuelle, B.; Bower, A.; Furey, H.; Hamilton, P. E.; Candela, J. Assessment of Numerical Simulations of Deep Circulation and Variability in the Gulf of Mexico Using Recent Observations. *Journal of Physical Oceanography* **2020**, *50*. https://doi.org/10.1175/JPO-D-19-0137.1.

Nowell, A. R. M.; Jumars, P. A.; Barnes, H.; Barnes, M. FLUMES : THEORETICAL AND EXPERIMENTAL CONSIDERATIONS FOR SIMULATION OF BENTHIC ENVIRONMENTS. In *Oceanography and Marine Biology: An Annual Review*; AberdeenUniversity Press, 1987; Vol. 25, p 23.

Passow, U.; Ziervogel, K.; Asper, V.; Diercks, A. Marine Snow Formation in the Aftermath of the Deepwater Horizon Oil Spill in the Gulf of Mexico. *Environ. Res. Lett.* **2012**, *7* (3), 035301. https://doi.org/10.1088/1748-9326/7/3/035301.

Passow, U.; Ziervogel, K. Marine Snow Sedimented Oil Released During the Deepwater Horizon Spill. *Oceanog* **2016**, *29* (3), 118–125. https://doi.org/10.5670/oceanog.2016.76.

Ravens, T. M.; Gschwend, P. M. Flume Measurements of Sediment Erodibility in Boston Harbor. *Journal of Hydraulic Engineering* **1999**, *125* (10), 998–1005. https://doi.org/10.1061/(ASCE)0733-9429(1999)125:10(998).

Romero, I. C.; Toro-Farmer, G.; Diercks, A.-R.; Schwing, P.; Muller-Karger, F.; Murawski, S.; Hollander, D. J. Large-Scale Deposition of Weathered Oil in the Gulf of Mexico Following a Deep-Water Oil Spill. *Environmental Pollution* **2017**, *228*, 179–189. https://doi.org/10.1016/j.envpol.2017.05.019.

Ross, C. B.; Gardner, W. D.; Richardson, M. J.; Asper, V. L. Currents and Sediment Transport in the Mississippi Canyon and Effects of Hurricane Georges. *Continental Shelf Research* **2009**, *29* (11), 1384–1396. https://doi.org/10.1016/j.csr.2009.03.002.

Sedflume Analysis Newtown Creek, New York; Sedflume Data Report; Sea Engineering, Inc., 2012; p 56.

Schwing, P. T.; Romero, I. C.; Brooks, G. R.; Hastings, D. W.; Larson, R. A.; Hollander, D. J. A Decline in Benthic Foraminifera Following the Deepwater Horizon Event in the Northeastern Gulf of Mexico. *PLOS ONE* **2015**, *10* (3), e0120565. https://doi.org/10.1371/journal.pone.0120565.

Schwing, P. T.; Romero, I. C.; Larson, R. A.; O'Malley, B. J.; Fridrik, E. E.; Goddard, E. A.; Brooks, G. R.; Hastings, D. W.; Rosenheim, B. E.; Hollander, D. J.; Grant, G.; Mulhollan, J. Sediment Core Extrusion Method at Millimeter Resolution Using a Calibrated, Threaded-Rod. *J Vis Exp* **2016**, No. 114. https://doi.org/10.3791/54363.

Smith, L. M.; Alexander, C.; Jennings, A. E. Accumulation in East Greenland Fjords and on the Continental Shelves Adjacent to the Denmark Strait over the Last Century Based on ^{210}Pb Geochronology. *Arctic* **2002**, *55* (2), 109–122.

Swarzenski, P. 210Pb Dating. In *Encyclopedia of Earth Sciences Series*; 2014; pp 1–11. https://doi.org/10.1007/978-94-007-6326-5_236-1.

Tesi, T.; Langone, L.; Ravaioli., M.; Giglio, F.; Capotondi, L. Particulate Export and Lateral Advection in the Antarctic Polar Front (Southern Pacific Ocean): One-Year Mooring Deployment. *Journal of Marine Systems* **2012**, *105–108*, 70–81. https://doi.org/10.1016/j.jmarsys.2012.06.002.

Thomsen, L.; Gust, G. Sediment Erosion Thresholds and Characteristics of Resuspended Aggregates on the Western European Continental Margin. *Deep Sea Research Part I: Oceanographic Research Papers* **1999**, *47* (10), 1881–1897. https://doi.org/10.1016/S0967-0637(00)00003-0.

Traynum, S.; Styles, R. Flow, Stress and Sediment Resuspension in a Shallow Tidal Channel. *Estuaries and Coasts* **2007**, *30* (1), 94–101. https://doi.org/10.1007/BF02782970.

Turnewitsch, R.; Falahat, S.; Nycander, J.; Dale, A.; Scott, R. B.; Furnival, D. Deep-Sea Fluid and Sediment Dynamics—Influence of Hill- to Seamount-Scale Seafloor

Topography. *Earth-Science Reviews* **2013**, *127*, 203–241. https://doi.org/10.1016/j.earscirev.2013.10.005.

Valentine, D. L.; Fisher, G. B.; Bagby, S. C.; Nelson, R. K.; Reddy, C. M.; Sylva, S. P.; Woo, M. A. Fallout Plume of Submerged Oil from Deepwater Horizon. *PNAS* **2014**, *111* (45), 15906–15911. https://doi.org/10.1073/pnas.1414873111.

Vonk, S. M.; Hollander, D. J.; Murk, A. J. Was the Extreme and Wide-Spread Marine Oil-Snow Sedimentation and Flocculent Accumulation (MOSSFA) Event during the Deepwater Horizon Blow-out Unique? *Marine Pollution Bulletin* **2015**, *100* (1), 5–12. https://doi.org/10.1016/j.marpolbul.2015.08.023.

Walsh, I.; Fischer, K.; Murray, D.; Dymond, J. Evidence for Resuspension of Rebound Particles from Near-Bottom Sediment Traps. *Deep Sea Research Part A. Oceanographic Research Papers* **1988**, *35* (1), 59–70. https://doi.org/10.1016/0198-0149(88)90057-X.

Ward, C. H. *Habitats and Biota of the Gulf of Mexico: Before the Deepwater Horizon Oil Spill: Volume 1: Water Quality, Sediments, Sediment Contaminants, Oil and Gas Seeps, Coastal Habitats, Offshore Plankton and Benthos, and Shellfish*; Springer, 2017.

Yan, B.; Passow, U.; Chanton, J. P.; Nöthig, E.-M.; Asper, V.; Sweet, J.; Pitiranggon, M.; Diercks, A.; Pak, D. Sustained Deposition of Contaminants from the Deepwater Horizon Spill. *PNAS* **2016**, *113* (24), E3332–E3340. https://doi.org/10.1073/pnas.1513156113.

Ziervogel, K.; Dike, C.; Asper, V.; Montoya, J.; Battles, J.; D′souza, N.; Passow, U.; Diercks, A.; Esch, M.; Joye, S.; Dewald, C.; Arnosti, C. Enhanced Particle Fluxes and

Heterotrophic Bacterial Activities in Gulf of Mexico Bottom Waters Following Storm-Induced Sediment Resuspension. *Deep Sea Research Part II: Topical Studies in Oceanography* **2016**, *129*, 77–88. https://doi.org/10.1016/j.dsr2.2015.06.017.